

Energy, environmental and economic analysis of the influence of the range of movement limit on horizontal single-axis trackers at photovoltaic power plants

A. Barbón^a, V. Carreira-Fontao^b, L. Bayón^c*, G. Spagnuolo^d

^a Department of Electrical Engineering, University of Oviedo, Spain

^b Polytechnic School of Engineering of Gijón, University of Oviedo, Spain

^c Department of Mathematics, University of Oviedo, Spain

^d Department of Information Engineering and Electrical Engineering and Applied Mathematics, University of Salerno, Italy

ARTICLE INFO

Handling Editor: Panos Seferlis

Keywords:

Horizontal single-axis tracker
Limit of motion
Analysis cost
Load analysis
CO₂ emissions

ABSTRACT

This paper presents a 3E (energy, environmental and economic) analysis of the impact of the movement limit on a horizontal single-axis tracker in Spain. Four scenarios have been analysed: (i) Scenario 1 (most favourable scenario), characterised by low wind and snow loads (Miraflores PV plant and Sueca location); (ii) Scenario 2, characterised by low wind and medium snow loads (Canredondo PV plant); (iii) Scenario 3, characterised by high wind and low snow loads (Basir PV plant); and (iv) Scenario 4 (less favourable scenario), characterised by high wind and snow loads (Rubió location). Four evaluation indicators (annual incident energy ratio, CO₂ emissions ratio, PV mounting system cost ratio, LCOE efficiency) and ten movement limits (β_{max}), ranging from $\pm 50^\circ$ to $\pm 60^\circ$, were analysed. Scenario 1 was used for comparison with the other scenarios. According to this study, the following conclusions can be drawn: (i) From an energetic point of view, the optimal maximum movement limit depends on each location; (ii) There is a relationship between CO₂ emissions and the presence of wind and snow loads. The higher the impact of wind and snow loads, the higher the CO₂ emissions. For example, in Scenario 4, the configurations $\beta_{max} = \pm 50^\circ$, $\beta_{max} = \pm 55^\circ$ and $\beta_{max} = \pm 60^\circ$ generate 1.94 (t/tracker), 2.07 (t/tracker) and 2.11 (t/tracker) more CO₂ emissions compared to Scenario 1; (iii) CO₂ emissions decrease with decreasing β_{max} . For example, in Scenario 4, the $\beta_{max} = \pm 60^\circ$ configuration generates 11.42% and 4.23% more CO₂ emissions compared to the $\beta_{max} = \pm 50^\circ$ and $\beta_{max} = \pm 55^\circ$ configuration, respectively; (iv) There is a relationship between the cost of the PV module mounting system and the presence of wind and snow loads. The higher the impact of wind and snow loads, the higher the cost of the PV module mounting system. For example, in Scenario 4, the configurations $\beta_{max} = \pm 50^\circ$, $\beta_{max} = \pm 55^\circ$ and $\beta_{max} = \pm 60^\circ$ the cost is higher by approximately 958 (€), 1034 (€) and 1045 (€) compared to Scenario 1; (v) The cost of the PV module mounting system decreases with decreasing β_{max} . For example, in Scenario 4, the $\beta_{max} = \pm 60^\circ$ configuration has a higher cost of 8.44% and 3.05% compared to the $\beta_{max} = \pm 50^\circ$ and $\beta_{max} = \pm 55^\circ$ configuration, respectively; and (vi) In all scenarios analysed, the LCOE efficiency was always lower for movement limits below $\beta_{max} = \pm 55^\circ$.

1. Introduction

The paradox of the energy sector lies in how it is necessary for the development of mankind and how it is responsible for the majority of greenhouse gas emissions (73% (UN, 2021)). One of the Sustainable Development Goals promoted by the United Nations is to ensure a sustainable future through the use of clean energy (UN, 2016). To this end, the electricity sector must transition from the use of fossil

fuels to clean energy. Within this framework, European Union (EU) countries have adopted policies to encourage the transition to clean and sustainable energy by promoting the use of clean energy in the energy sector. Several EU Member States have established targets to achieve net zero emissions by 2050 (IEA, 2023). These policies have led to a substantial increase in the use of clean energies such as wind, solar, etc. in the energy sector (EI, 2023). Lower production costs and policies

* Corresponding author.

E-mail addresses: barbon@uniovi.es (A. Barbón), carreirafontao@gmail.com (V. Carreira-Fontao), bayon@uniovi.es (L. Bayón), gspagnuolo@unisa.it (G. Spagnuolo).

<https://doi.org/10.1016/j.jclepro.2024.144637>

Received 25 September 2024; Received in revised form 1 December 2024; Accepted 30 December 2024

Available online 6 January 2025

0959-6526/© 2025 Elsevier Ltd. All rights are reserved, including those for text and data mining, AI training, and similar technologies.

Nomenclature table

A_{PV}	Photovoltaic module area (m^2)
AIE	Annual incident energy on the PV field (kWh/m^2)
$AIEC$	Comparison of the annual incident energy on the PV field (%)
$AIER$	Annual incident energy rate (dimensionless)
C_e	Exposure factor
C_i	Initial investment cost (€)
C_{OM}	Cost of operation and maintenance (€)
C_p	Pressure coefficient
C_{prob}	Probability factor
C_{PV}	Unit cost of a PV module (€/unit)
CMS	Cost of the PV mounting system (€)
CO_2ER	Cost of the PV mounting system ratio (dimensionless)
CO_2E	CO_2 emissions (t)
CO_2ER	CO_2 emissions ratio (dimensionless)
d	Distance $E - W$ between two adjacent mounting systems (m)
d_r	Annual degradation rate
d_{min}	Minimum distance $E - W$ between two adjacent mounting systems (m)
d_{st}	Standard distance $E - W$ between two adjacent mounting systems (m)
E_i	Total electrical energy output at the i th year (kWh)
e_l	Distance $N - S$ between two adjacent mounting systems (m)
e_s	Minimum distance on the ground (m)
e_t	Pitch (m)
H_i	Solar irradiation at the i th year (Wh/m^2)
H_t	Total irradiation on a tilted surface (Wh/m^2)
I_{bh}	Beam irradiance on a horizontal surface (W/m^2)
I_{dh}	Diffuse irradiance on a horizontal surface (W/m^2)
I_t	Total irradiance on a horizontal surface (W/m^2)
i	Year number ranging (years)
L	Length of the mounting system (m)
L_{PV}	Length of the photovoltaic modules (m)
$LCOE$	Levelised cost of electricity (€/kWh)

$LCOE$	Ratio between the $LCOEs$ rack configurations
Efficiency	Lifetime of the project (years)
N	Normal Operating Cell Temperature ($^{\circ}C$)
$NOCT$	Ordinal of the day (day)
n	Power generated by a PV module (W/m^2)
P_{PV}	Height of the column (m)
p	Basic velocity pressure (kN/m^2)
q_b	Static pressure (kN/m^2)
q_e	Load due to the weight of the PV modules (kN/m^2)
q_{PV}	Discount rate for i th year
r	Snow load (kg)
S_L	Solar time (h)
T	Sunrise solar time (h)
T_R	Sunset solar time (h)
T_S	End of the backtracking mode (h)
T_{b1}	Start of the backtracking mode (h)
T_{b2}	Start of the normal tracking mode (h)
$T_{\beta 1}$	End of the normal tracking mode (h)
$T_{\beta 2}$	Ambient temperature ($^{\circ}C$)
T_a	PV cell temperature ($^{\circ}C$)
T_c	Reference temperature ($^{\circ}C$)
T_{ref}	Basic wind velocity (m/s)
v_b	Width of the mounting system (m)
W	Weight of the PV module (kg)
$W_{e,PV}$	Weight of the structure (kg)
$W_{e,S}$	Wind load (kg)
W_L	Width of the photovoltaic modules (m)
W_{PV}	Absorbance of the photovoltaic coating (dimensionless)
α	Tilt angle of photovoltaic module ($^{\circ}$)
β	Backtracking angle ($^{\circ}$)
β_B	Limited range of motion angle ($^{\circ}$)
β_{max}	Temperature coefficient of the PV module ($1/^{\circ}C$)
β_{ref}	Standard tilt angle of photovoltaic module ($^{\circ}$)
β_{st}	Azimuth angle of photovoltaic module ($^{\circ}$)
γ	Azimuth of the Sun ($^{\circ}$)
γ_S	Solar declination ($^{\circ}$)
δ	Electrical efficiency (dimensionless)
η_e	Reference electrical efficiency (dimensionless)
η_{ref}	Incidence angle ($^{\circ}$)
θ_i	Transversal angle ($^{\circ}$)
θ_t	Standard transversal angle ($^{\circ}$)
θ_{1st}	Zenith angle of the Sun ($^{\circ}$)
θ_z	Ground reflectance (dimensionless)
ρ_g	Transmittance of the glazing (dimensionless)
τ	Hour angle ($^{\circ}$)
ω	

aimed at promoting the use of less carbon-intensive energy sources are the main reasons for this change.

Renewable energy growth is led by wind and solar power. The continued reduction in the levelised cost of energy ($LCOE$) of photovoltaic (PV) systems supports the strong increase in their use. Forecasts by the International Energy Agency (IEA) show that solar energy will play a predominant role in power generation over the next decade (IEA , 2023). The evolution of the cumulative installed capacity of PV systems is shown in Fig. 1 ($IRENA$, 2023). The techno-economic performance of PV power plants has increased with the introduction of tracking systems (Racharla and Rajan, 2017). This has driven the global market for solar trackers. In 2022, this market was valued at USD 3.2 billion (FMI , 2023). It is estimated that the market will grow at an average annual rate of 7.5% until 2033, when the market value will be around USD 7.2 billion (FMI , 2023).

These systems can be implemented in two main configurations based on the degrees of freedom set on the solar tracker: (i) dual-axis trackers (two degrees of freedom), and (ii) single-axis trackers (one degree of freedom). Dual-axis trackers produce the most energy (Barbón et al., 2021). However, they have higher operation and maintenance costs (Martín-Martínez et al., 2019). In contrast, single-axis trackers produce less energy (Barbón et al., 2021), but have lower maintenance and operating costs (Martín-Martínez et al., 2019). Nowadays,

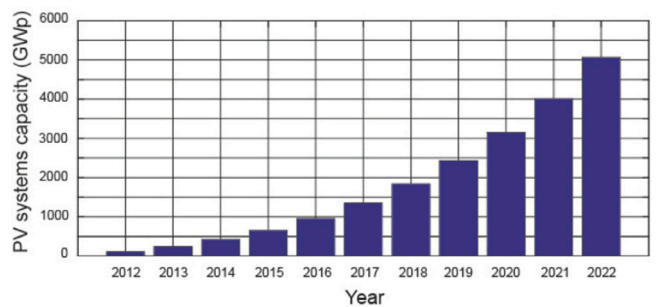


Fig. 1. The capacity of installed PV systems worldwide.

commercial-scale *PV* power plants almost exclusively use single-axis trackers (FMI, 2023). Although there are different configurations for these solar trackers, horizontal single-axis trackers (a single-axis tracker configuration with horizontal North–South axis and East–West tracking) are the most commonly used configuration (FMI, 2023). Therefore, this study focused on horizontal single-axis trackers.

1.1. Literature review

The increase in the implementation of *PV* systems worldwide has focused the study on increasing the energy efficiency of these systems. This study can be carried out from various points of view. In this context, the development of photovoltaic technology, driven by scientific research in this field, is reaching high levels of optimisation allowing this technology to become an alternative energy source to fossil fuels. The optimisation of *PV* power plants is fundamental to the decision-making process for the installation of these plants.

To show the novelty of this work, a literature search has been carried out from three points of view: (i) studies that take into account the limit of movement of the solar tracker, (ii) studies that take into account wind loads, and (iii) works that carry out 3E (Energy, Environment and Economics) studies.

Some of the most relevant publications that take into account the limit of movement of the solar tracker are reviewed below:

- (i) Keiner et al. (2024) analysed four backtracking strategies to improve the techno-economic performance of horizontal single-axis trackers. This work used a movement limit of ± 50 ($^{\circ}$). This study did not take into account the effect of the solar tracker movement limit.
- (ii) A methodology was presented in Barbón et al. (2023a) to facilitate the optimisation of *PV* power plants with horizontal single-axis trackers. Equations were developed based on design variables such as irregular land shape, mounting system size and configuration, row spacing and periods of operation to determine of optimal row spacing and periods of operation. A packing algorithm that takes into account the irregular shape of the land and possible mounting system configurations was also presented. This work used a movement limit of ± 60 ($^{\circ}$), without analysing the influence of this parameter.
- (iii) Casares de la Torre et al. (2022) presented a study on the conversion of *PV* power plants with horizontal single-axis trackers at agricultural locations by growing trees in hedgerows between the rows of trackers. In this study, a movement limit of ± 55 ($^{\circ}$) was used, without examining the effect of this variable.
- (iv) Alves Veríssimo et al. (2020) presented an optimised design for *PV* power plants, with horizontal single-axis trackers based on a new evaluation metric called Y_{AREA} , which represents the annual energy yield normalised by the surface area of the *PV* power plant. This study did not take into account the movement limit.

These advances in *PV* power plant design consider the constant movement limit, but the influence of this parameter on other *PV* power plant design parameters was never considered. Consequently, the optimal development of these advances in *PV* power plant design has not yet been achieved.

Table 1 shows the technical characteristics of several *PV* power plants in Spain (all using horizontal single-axis trackers). As can be seen, the vast majority of them use ± 60 ($^{\circ}$) as the movement limit. Certain doubts arise with regard to this choice: (i) is this movement limit suitable for all locations; and (ii) is this movement limit suitable for the wind loads at all locations? It is for these reasons that this study aims to show the influence of this parameter on the incident energy, the CO_2 emissions, the *LCOE* and the cost of a *PV* mounting system.

Another fundamental aspect is the assessment of wind loads, as they cause a multitude of incidents with high economic costs (Gcube, 2024). A failure to properly assess the movement limit of a horizontal

single-axis tracker leads to wind-related structural failures and thus to frustrated *PV* systems, dissatisfied customers, and high unforeseen costs. In addition, uncertainty about what constitutes a safe *PV* systems for a given movement limit of a horizontal single-axis tracker can halt the legalisation process of a *PV* plant and complicate the commissioning of the plant. This fact is corroborated by numerous studies on the aerodynamic forces on heliostats or *PV* modules:

- (i) Martínez-García et al. (2021) presented an analytical and experimental study on how module inertia and panel aspect ratio influence the onset of torsional galloping. This study also includes the effect of torsional tube stiffness. The study only took into account a single limiting angle of movement.
- (ii) Stathopoulos et al. (2014) presented an experimental study to better understand the wind pressure distribution on free-standing panel surfaces and panels attached to flat roofs of buildings. Systems with solar trackers were not the subject of this study.
- (iii) Strobel and Banks (2014) presented a study on the fundamental natural frequency of wind loads impinging on *PV* modules. The *PV* module mounting system used in this study had a fixed tilt angle. Systems with solar trackers were not the subject of this study.
- (iv) Pfahl et al. (2018) presented a study on wind load coefficients on heliostats. To this end, they analysed the incidence of wind loads on a heliostat with two rotational movements. Systems with single-axis solar trackers were not the subject of this study.

Several aspects must be taken into account in the *PV* power plant design decision-making process, such as technical, environmental and economic aspects. Technical optimisation complemented by a levelised cost of energy (*LCOE*) assessment leads to economic optimisation. Therefore, in order to make progress in this field, different aspects need to be analysed simultaneously such as energy, environmental, mechanical, economic, etc. The specialised literature shows a multitude of studies, in the field of solar energy, related to the 3E (Energy, Environment and Economics) analysis of various technologies and parameters. Several of these studies are shown below:

- (i) Mohammed et al. (2024) presented a study on the properties and performance of paraffin, natural beeswax and a combination of both, compared to a solar panel lacking any phase change substance. The experiment was conducted in the city of Hawija, Iraq. The *PV* module mounting system used had a fixed tilt angle.
- (ii) Yusuf and Astiaso Garcia (2023) presented an energy, economic and environmental (4E) analysis of two conventional unifacial photovoltaic–thermoelectric systems and two bifacial photovoltaic–thermoelectric systems. Due to the nature of the study, single-axis solar trackers were not studied.
- (iii) Alomar et al. (2023) presented an investigation on the energy, exegetic, economic and environmental analysis of a solar *PV* system using three different types of *PV* mounting systems: fixed tilt angle system, single-axis tracking system, and dual-axis tracking system. The study was conducted at a single location, the city of Zakho (northern Iraq). This study does not take into account the limit of motion in the solar trackers.
- (iv) Ali and Alomar (2023) presented a techno-economic study to evaluate the productivity of a grid-connected solar *PV* system on a campus of Zakho University, Iraq. The study was conducted at a single location. This study uses fixed tilt angle mounting systems, therefore does not take into account the limit of movement of the solar trackers.
- (v) Yousef et al. (2022) presented a study on the thermal regulation of a *PV* system using a paraffin/aluminium foam composite. The experiments were carried out in the city of Benha, Egypt. The systems analysed used fixed tilt-angle *PV* mounting systems.

Table 1
Specifications of the PV power plants assessed in this study.

PV power plant	Location	Latitude	Longitude	Altitude (m)	Power (MWp)	Motion limit (°)
Canredondo	Guadalajara	40°47'58.886"N	2°31'26.95"W	1162	21.98	±60
Campos de Teruel	Teruel	40°47'35.60"N	2°46'37.23"E	1292	25	±60
Plato	Madrid	40°22'18.92"N	3°19'46.99"W	809	22.58	±60
Miraflores	Badajoz	38°46'4.8"N	5°32'49.199"W	1162	22	±60
Jumilla	Murcia	38°27'14.48"N	1°16'42.94"W	510	8.9	±55
Campos	Murcia	38°3'42.25"N	1°23'27.23"W	172	109.19	±60
Mula II	Murcia	37°59'24.21"N	1°24'41.90"W	313	114.4	±60
Yarte	Cádiz	36°36'21.96"N	5°47'55.68"W	143	50	±60
Basir	Cádiz	36°20'24"N	5°50'32.6"W	104	20.013	±60

- (vi) Ali et al. (2022) presented a study on the energy, economic and environmental performance of a 1 MWp PV power plant in the city of Zakho/Iraq. This study does not take into account the movement limit of the solar trackers.
- (vii) Yaghoubirad et al. (2022) presented a multi-criteria study consisting of energy, exergy, economic and environmental analyses of a PV module to investigate the influence of climatic conditions on the module's performance. For this purpose, six cities with six different climates in the USA were chosen. The PV module mounting system used had a fixed tilt angle.

Based on the literature search, it can be concluded that there are no 3E (energy, environmental, and economic) studies in the literature that take into account the influence of the movement limit of a horizontal single-axis tracker. This is the main objective of this work: to analyse the movement limit parameter from various points of view.

1.2. Scientific contributions

In this paper, we provide energy, environmental, and economic analyses of the influence of the movement limit of a horizontal single-axis tracker on three active PV power plants in Spain as well as two locations in Spain that meet the most stringent and most beneficial conditions in terms of wind and snow loads. For this purpose, we rely on the CTE (Technical Building Code) (STBC, 2006) for the calculation of structures under different wind and snow load conditions. Although a multitude of parameters are involved in the design of a PV plant, we focus only on the movement limit of a horizontal single-axis tracker. Another reason for choosing a certain movement limit is to reduce the cost of electricity generated. Common questions such as "how much does it cost" and "is it profitable" are answered by calculating the cost of electricity production. The levelised cost of electricity (LCOE) method can be used to do so. The main contributions of this work are as follows:

- To present a comprehensive study on the movement limit of a horizontal single-axis tracker when attempting to optimise the incident energy in the PV field at each location since the value generally used at PV power plants of ± 60 (°) is not optimal for certain locations. This also involves quantifying the energy loss associated with the choice of movement limit.
- To analyse the relationship between wind and snow loads on the CO₂ emissions produced when manufacturing a structure as concerns the movement limit on a solar tracker.
- To analyse the influence of the movement limit adopted at a PV power plant on the cost of the solar tracker structure.
- To analyse the influence of the movement limit adopted at a PV power plant on the levelised cost of electricity.
- To develop of several specific codes using *Mathematica*[™] software for a detailed analysis of the movement limit of a horizontal single-axis tracker as it is not possible to carry out this study in depth using the commercial software currently available.

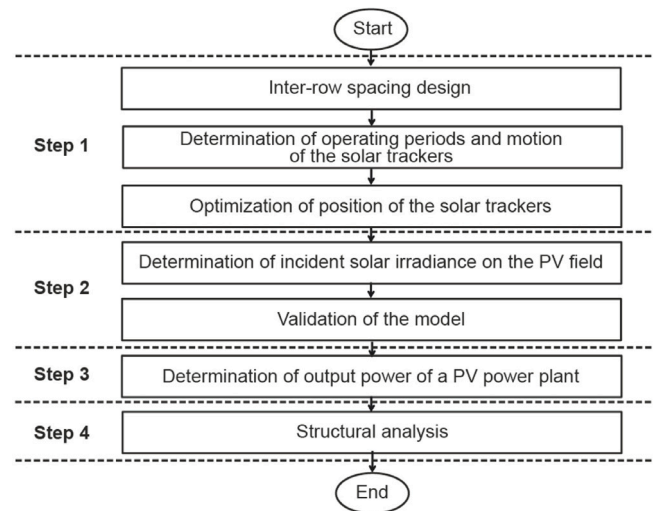


Fig. 2. A flowchart outlining the proposed methodology.

In summary, the aim of this work is to facilitate decision-making when choosing the movement limit for a horizontal single-axis tracker in a PV power plant design.

The remainder of the paper is organised as follows: Section 2 shows the modelling of a PV power plant with horizontal single-axis trackers, including: row spacing design, periods of operation, power output, model validation and a structural analysis of a PV mounting system. The detailed formulation of the problem is presented in Section 3. Section 4 presents the limitations of the study. Section 5 presents the assessment indicators used. Section 6 presents the results obtained at five locations in Spain. Finally, the main conclusions of this work are drawn in Section 7.

2. Modelling a PV power plant with horizontal single-axis trackers

This section presents the procedure used in the study.

In order to achieve the objectives of this study, it is necessary to use a methodology that allows the modelling of a PV power plant with horizontal single-axis trackers. For this purpose, a series of steps have to be followed: (i) PV power plant design; (ii) Determination of incident solar irradiance on the PV field; (iii) Determination of the power output of the PV power plant; and (iv) Structural analysis of a PV mounting system. In turn, in step (i), the following parameters need to be optimised (Barbón et al., 2023a): inter-row spacing, solar tracker periods of operation, and the optimal number of solar trackers. Fig. 2 shows a flow chart summarising the proposed methodology.

2.1. PV power plant design

When attempting to find the optimal design of a PV power plant for a given location, a set of constraints must be taken into account,

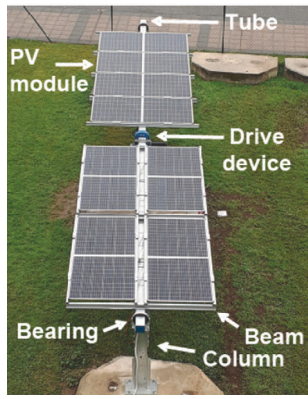


Fig. 3. Photograph of horizontal single-axis tracking.

such as Barbón et al. (2023a): the available area of land, the shape of the land, the orography of the land, the configuration of the mounting system (dual-axis tracking, single-axis tracker, fixed tilt angle), and the commercial PV module model. In addition, the modelling of a PV power plant involves several fields of expertise, such as electrical and mechanical.

As the single-axis tracker configuration with horizontal North–South axis and East–West tracking (know as “horizontal single-axis tracking”) is the most commonly used in practice (FMI, 2023), this PV mounting system will be the one used in this study. A horizontal single-axis tracker consists of a North–South oriented torsion tube on which the PV modules are mounted. This tube is supported by several intermediate columns fitted with spherical bearings that allow free rotation. An electric motor (DC motor and drivers) transmits the rotational movement to the torsion tube. Fig. 3. shows a photograph of a horizontal single-axis tracker.

Once the PV mounting system (in this case, a horizontal single-axis tracker) has been selected, a large number of parameters are involved in the design of a PV power plant. The parameters related to the land are: the available surface, the shape and the orography. These parameters influence the number of PV modules at a PV power plant. Some of them are related to the chosen PV module: the maximum output power, the length of the PV module (L_{PV}), and the width of the PV module (W_{PV}). These two parameters influence the design of the PV mounting system, e.g. the length of a PV mounting system (L), the width of a PV mounting system (W), the height of the column (p), the minimum ground clearance (e_s), and the maximum tilt angle (β_{max}). Other parameters are related to the correct operation of the plant, i.e. avoiding shading between PV modules by choosing the right $E - W$ distance between columns of two adjacent mounting systems (pitch) (e_t), facilitating maintenance and cleaning by choosing the minimum $E - W$ distance between two adjacent mounting systems (d_{min}), facilitating maintenance by choosing the minimum $N - S$ distance between adjacent mounting systems (e_l), and maximising the solar irradiation incident on the PV modules by choosing the appropriate tilt angle for the PV modules (β). Fig. 4 shows these parameters. β is determined for each solar tracker period of operation and e_t is determined by the optimal inter-row spacing design.

Once the constraints have been set, the following parameters need to be optimised (Barbón et al., 2023a): inter-row spacing, solar tracker periods of operation, and the optimal number of solar trackers. The power output can be determined once the PV power plant has been optimised.

2.1.1. Inter-row spacing design

Avoiding the shading of PV cells is essential to preventing an increase in the temperature of the cell and the appearance of hot spots (Belhachat and Larbes, 2015), which can lead to the deterioration of

Table 2

Cases in the determination of pitch (e_t).

Case	Pitch	Specifications	
A1	$e_t = d_{st} + W \cos \theta_{lst}$	$\theta_{lst} \leq \beta_{max}, d_{st} \geq d_{min}$	$d_{st} = W \frac{\sin^2 \theta_{lst}}{\cos \theta_{lst}}$
A2a	$e_t = d_{min} + W \cos \theta_{ld}$	$\theta_{lst} \leq \beta_{max}, d_{st} < d_{min}, \theta_{st} < \theta_{lst}$	$d_{st} = W \frac{\sin^2 \theta_{lst}}{\cos \theta_{lst}}$
A2b	$e_t = d_{min} + W \cos \beta_{max}$	$\theta_{lst} \leq \beta_{max}, d_{st} < d_{min}, \theta_{st} > \theta_{lst}$	$d_{st} = W \frac{\sin^2 \theta_{lst}}{\cos \theta_{lst}}$
B1	$e_t = d_{st} + W \cos \beta_{max}$	$\theta_{lst} > \beta_{max}, d_{st} \geq d_{min}$	$d_{st} = W \tan \theta_{lst} \sin \beta_{max}$
B2	$e_t = d_{min} + W \cos \beta_{max}$	$\theta_{lst} > \beta_{max}, d_{st} < d_{min}$	$d_{st} = W \tan \theta_{lst} \sin \beta_{max}$

the cell. Therefore, e_t must be calculated so that shading losses are minimised. For this, three constraints have to be fulfilled simultaneously: β_{max} , d_{min} , and θ_{lst} . The first two parameters have already been defined.

Several technical reports show the procedure for determining θ_{lst} . One of these reports issued by the Spanish Government’s Institute for Energy Diversification and Savings (IDAR, 2011) states that a minimum of four hours of sunshine around noon without shadows between PV modules must be guaranteed during the winter solstice. In other words, θ_{lst} is determined for 21 December at 10 : 00 a.m. by the equation (Barbón et al., 2023a):

$$\theta_{lst} = \arctan(\tan \theta_z |\sin \gamma_s|) \quad (1)$$

where θ_z is the zenith angle of the Sun ($^\circ$), and γ_s is the azimuth of the Sun ($^\circ$).

The procedure for determining e_t can be found in Barbón et al. (2023a). Five different cases can be given depending on β_{max} , d_{min} , and θ_{lst} . Table 2 shows these cases.

2.1.2. Horizontal single-axis tracker periods of operations

The solar algorithm implemented in an electronic control system governing the electric motor consists of three operation periods: (i) normal tracking mode, (ii) backtracking mode, and (iii) static mode (in a limited movement position).

With the solar tracker in backtracking mode, the solar tracker starts with tracking angles close to 0 ($^\circ$) at sunrise. As the solar altitude increases, the solar tracker tracks West–East until it reaches the movement limit ($-\beta_{max}$). Although the Sun is above the movement limit, the tracker remains at this limit (static mode). Once in normal tracking mode, the solar tracker follows the Sun during the day from East to West until it reaches the movement limit ($+\beta_{max}$) (static mode). Then the backtracking mode begins until sunset.

Normal tracking mode

The normal tracking mode is characterised by the PV modules rotating from East to West on a horizontal torsion tube, following the daily movement of the Sun. This movement is determined by algorithms that predict the position of the Sun on the celestial sphere with high accuracy. Some of these algorithms and their accuracy are shown in Table 3. The objective of the normal tracking mode is to maximise the incident solar irradiance on the PV module. For this purpose, the solar algorithm implements astronomical solar tracking that seeks to minimise the angle of solar incidence on the vector normal to the PV module (Duffie and Beckman, 2013). This minimisation is obtained when the rotation of the solar tracker coincides with the projection of the Sun’s position on the plane of rotation. Therefore the electric motor drives the torsion tube during the day to track the solar altitude by means of a discrete movement. This means that the photovoltaic modules will be in a horizontal position at noon.

The angle that needs to be determined in this period of operation is the tilt angle (β). This angle can be determined by the equation (Duffie and Beckman, 2013):

$$\beta = \theta_t = \arctan(\tan \theta_z |\sin \gamma_s|) \quad (2)$$

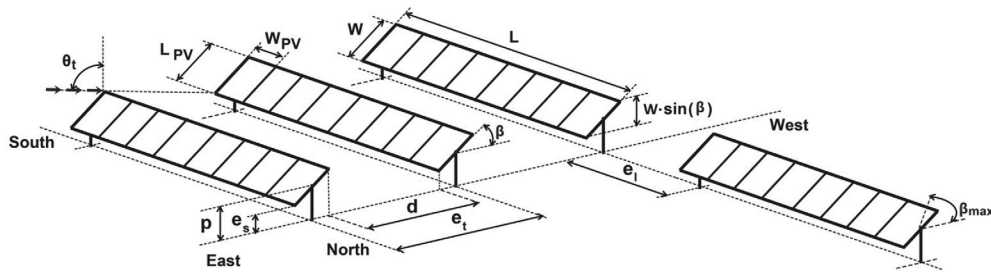


Fig. 4. Parameters of a PV power plant.

Table 3
Algorithms for determining the position of the Sun in normal tracking mode.

Algorithm	Maximum error (°)
Int. Solar Position Algorithm (SPA) (Reda and Andreas, 2004)	0.0003
Michalsky (1988)	0.01
Blanco-Muriel et al. (2001)	0.008
Grena Algorithm (Grena, 2008)	0.0027

where θ_t is the solar transversal angle (°), θ_z is the zenith angle of the Sun (°), and γ_s is the azimuth of the Sun (°).

Backtracking mode

Avoiding self-shading between PV modules is the main premise of the solar tracking algorithm. Self-shadowing occurs when the solar elevation is low (sunrise and sunset). A technique called backtracking is utilised to avoid this (Casares de la Torre et al., 2022). The backtracking mode does not achieve maximum solar irradiance incidence, but avoids shading between PV modules and thus the negative effect of hot spots (Antonanzas et al., 2018).

The angle that needs to be determined in this period of operation is the backtracking angle (β_B). This angle can be determined by the equation (Barbón et al., 2023a):

$$\beta_B = \theta_t - \arccos\left(\frac{e_t}{W} \cos \theta_t\right) \quad (3)$$

Static mode (limited range of movement)

A horizontal single-axis tracker has a limited range of movement. This range depends on the manufacturer and is usually $\pm 60^\circ$ (Gonvarri, 2024). This maximum angle is related to the wind loads that the PV modules can withstand. The parameter to be set is the maximum tilt angle (β_{max}). Fig. 5 shows a representation of the periods of operation of a horizontal single-axis tracker.

In the most general case, there are 5 zones of operation with the following sequence: (i) sunrise backtracking mode (T_R, T_{b1}), (ii) limited range of movement ($T_{b1}, T_{\beta1}$), (iii) normal tracking mode ($T_{\beta1}, T_{\beta2}$), (iv) limited range of movement ($T_{\beta2}, T_{b2}$), and (v) sunset backtracking mode (T_{b2}, T_S), where T_R is the sunrise solar time (h), T_{b1} is the end of the sunrise backtracking mode (h), $T_{\beta1}$ is the start of the normal tracking mode (h), $T_{\beta2}$ is the end of the normal tracking mode (h), T_{b2} is the start of the sunset backtracking mode (h), and T_S is the sunset solar time (h).

In Fig. 5a, the backtracking mode ends without reaching the movement limit. In other words, it goes directly to the normal tracking mode. In contrast, Fig. 5b reflects a waiting time at the position of the movement limit. These two possibilities will influence the incident energy on the PV field.

2.1.3. Optimal number of solar trackers

In addition to the solar tracking strategies used, there are other parameters to be considered when designing a PV power plant, such as: (i) the available area of land, (ii) the shape of the land, and (iii) the orography of the land, which influence the energy produced. Packing algorithms are used to take these parameters into account

when designing a PV power plant (Barbón et al., 2023a). This study focuses on the influence of the movement limit on the solar tracking strategies as the three previous parameters are not considered because the PV power plants analysed are already active.

2.2. Incident solar irradiance on the PV field of a PV power plant

The hourly incident solar irradiance on PV modules can be determined by Eq. (4) (Duffie and Beckman, 2013):

$$I_t(n, \beta, T) = I_{bh}(n, T) \cdot \frac{\cos \theta_t}{\cos \theta_z} + I_{dh}(n, T) \cdot \left(\frac{1 + \cos \beta}{2}\right) + (I_{bh}(n, T) + I_{dh}(n, T)) \cdot \rho_g \cdot \left(\frac{1 - \cos \beta}{2}\right) \quad (4)$$

where $I_t(n, \beta, T)$ is the hourly incident solar irradiance on PV modules (W/m^2), $I_{bh}(n, T)$ is the beam solar irradiance on a horizontal surface (W/m^2), $I_{dh}(n, T)$ is the diffuse solar irradiance on a horizontal surface (W/m^2), n is the day of the year (day), β is the tilt angle (°), θ_z is the zenith angle of the Sun (°), ρ_g is the ground reflectance (dimensionless), T is the solar time (h), and θ_t is the incident angle (°). The following considerations must be taken into account when using Eq. (4):

- (i) According to Eq. (4) the $I_t(n, \beta, T)$ consists of three summands: beam irradiance, diffuse irradiance and ground-reflected irradiance. A separate understanding of each of these summands is important in this study.
- (ii) The determination of the beam irradiance is uncomplicated as it uses equations based on astronomy (Duffie and Beckman, 2013). The incident angle θ_t must be determined for each period of operation (see Fig. 3). For this purpose, the following equations can be used (Duffie and Beckman, 2013):

- Normal tracking mode:

$$\cos \theta_t = \sqrt{\cos^2 \theta_z + \cos^2 \delta \sin^2 \omega} \quad (5)$$

- Backtracking mode:

$$\cos \theta_t = \cos \beta_B \cos \theta_z + \sin \beta_B \sin \theta_z \cos(\gamma_s - \gamma) \quad (6)$$

- Limited range of movement:

$$\cos \theta_t = \cos \beta_{max} \cos \theta_z + \sin \beta_{max} \sin \theta_z \cos(\gamma_s - \gamma) \quad (7)$$

where β is the tilt angle in normal tracking mode (°), θ_z is the zenith angle of the Sun (°), δ is the solar declination (°), ω is the hour angle (°), β_B is the tilt angle in backtracking mode (°), γ_s is the azimuth of the Sun (°), γ is the azimuth angle (°), and β_{max} is the tilt angle in a limited range movement (°).

- (iii) The determination of diffuse irradiance is complex and different models can be used (Duffie and Beckman, 2013). Some of these models include: the Liu–Jordan isotropic model (Liu and Jordan, 1963), the Hay–Davies anisotropic model (Hay, 1993), and the Perez’s anisotropic model (Perez et al., 1990), etc. These three

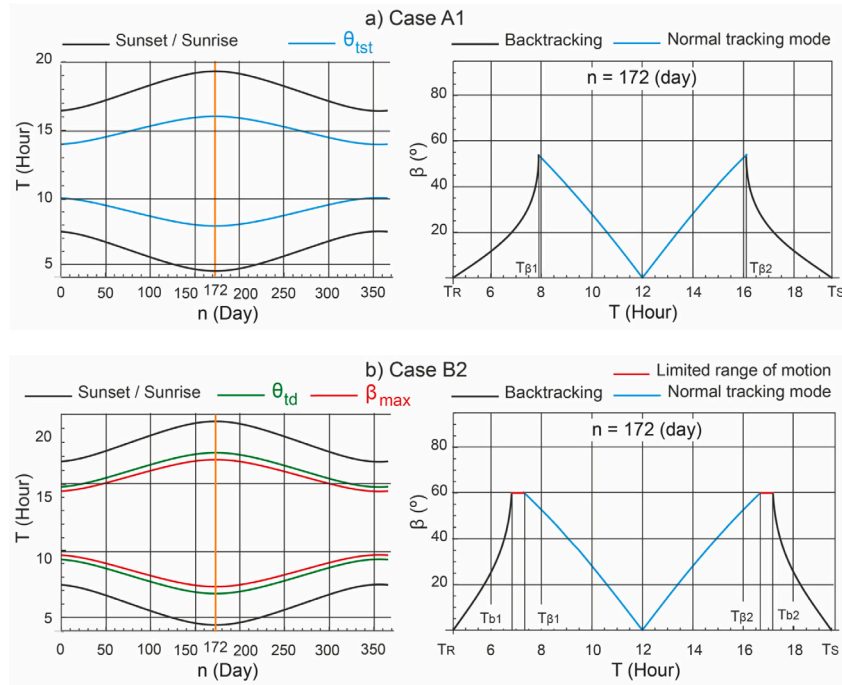


Fig. 5. Representation of the horizontal single-axis tracker periods of operation.

models were compared in a study on horizontal single-axis solar trackers with similar results (Casares de la Torre et al., 2022). The study presented by Mehleri et al. (2010), in which they compared isotropic (4) and anisotropic (7) models, also concluded that the Liu–Jordan isotropic model gave more accurate results. Liu–Jordan isotropic model (Liu and Jordan, 1963) is based on the assumption that the diffuse irradiance is uniform over the sky. This model has been used in a multitude of studies in different parts of the world. For example, López et al. (2022) used the Liu–Jordan isotropic model in Spain, Makhdoomi and Askarzadeh (2021) in Iran, and Zhu et al. (2020) in China. It is therefore appropriate to assume that the use of this simplified model is adequate for this study. The Liu–Jordan isotropic model is used in Eq. (4).

- (iv) Due to the large number of factors influencing the ground-reflected irradiance it is conceptually impossible to calculate this accurately (Duffie and Beckman, 2013) and therefore most authors consider it to be isotropic. Based on this assumption, Liu and Jordan (1963) propose an equation used by most authors. For example, Perez et al. (1990) used the equation proposed by Liu and Jordan in their research on isotropic solar irradiance models, Hay (1993) also used this equation in his isotropic solar irradiance model, Makhdoomi and Askarzadeh (2021) used this equation in their study on the sizing of hybrid energy systems, Zhu et al. (2020) used this equation in their study on a novel single-axis tracking structure to maximise energy harvesting.
- (v) The most important parameters of Eq. (4) are: the I_{bh} and I_{dh} (Duffie and Beckman, 2013). As is well known, I_{bh} and I_{dh} are site-specific, as they are significantly affected by the local distribution of cloudiness (Armstrong and Hurley, 2010). Although ground-level meteorological stations provide reliable values for these two irradiances, the number of such stations globally is very low. Although ground-level weather stations provide reliable values for these two irradiances, the number of such stations worldwide is very low. Therefore, it is safe to say that the probability that a weather station is available at the location of the PV power plant is very low. Therefore, models have to be used to estimate I_{bh} and I_{dh} . There are a large number of models based

on different techniques that can be used: clear sky models (Zhu et al., 2020), satellite-based models (Salazar et al., 2020), etc. This study uses a model that takes into account the meteorological conditions at each location (Barbón et al., 2020). This model has been used in similar work such as: the optimal design of single-axis tracking PV power plants (Barbón et al., 2023a), the experimental and numerical investigation of the influence of terrain slope on the performance of single-axis trackers (Barbón et al., 2023b), and in the use of an artificial neural network based on learning algorithms for solar irradiance prediction (Jallal et al., 2020). This procedure consists of the following steps (Barbón et al., 2020): (1) Determination of the beam solar irradiance on a horizontal surface ($I_{bh}(n, T)$). For this, the Hottel clear-sky model (Hottel, 1976) is used; (2) Determination of the diffuse solar irradiance on a horizontal surface ($I_{dh}(n, T)$). For this, the Liu and Jordan clear-sky model (Liu and Jordan, 1960) is used; (3) Reduction of the clear day models from steps 1 and 2 to the meteorological conditions at the site. For this, this procedure uses monthly-averaged beam and diffuse solar irradiation for the site under study, averaged over a 10-year period, obtained by satellite from the PVGIS database (PVGIS, 2024).

The incident solar irradiation on the PV field ($H_t(n)$) can be determined by Eq. (8), which takes into account the incident solar irradiance each day of the year (n) and the 5 operating zones, which is the most general case (Barbón et al., 2023a):

$$\begin{aligned}
 H_t(n) = & \int_{T_R(n)}^{T_{\beta_1}(n)} I_t(n, \beta_B, T) dT + \int_{T_{\beta_1}(n)}^{T_{\beta_1}(n)} I_t(n, -\beta_{\max}, T) dT \\
 & + \int_{T_{\beta_1}(n)}^{T_{\beta_2}(n)} I_t(n, \theta_i, T) dT + \int_{T_{\beta_2}(n)}^{T_{\beta_2}(n)} I_t(n, \beta_{\max}, T) dT \\
 & + \int_{T_{\beta_2}(n)}^{T_S(n)} I_t(n, \beta_B, T) dT
 \end{aligned} \tag{8}$$

Only a fraction of the solar irradiance incident on the PV modules is converted into electricity, the rest is converted into heat. Eq. (9) can be used to determine the power generated by a PV module (P_{PV}) (Skoplaki and Palyvos, 2009):

$$P_{PV} = (\tau \cdot \alpha) \cdot I_t \cdot \eta_e \tag{9}$$

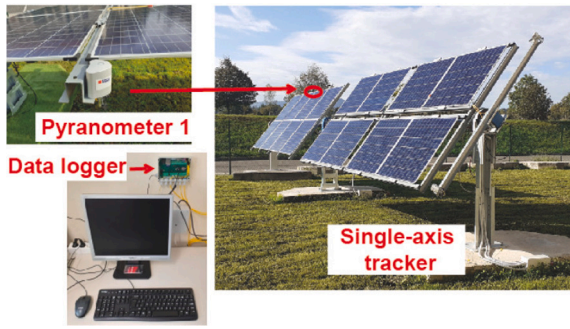


Fig. 6. Configuration of the experimental system.

where $\tau \cdot \alpha$ is the product of the transmittance of the glazing and the absorbance of the photovoltaic coating (dimensionless), often estimated to be 0.9 (Kalogirou et al., 2013), I_t is the incident solar irradiance on *PV* modules (W/m^2), and η_e is the electrical efficiency of the module to convert the incident solar irradiance into electrical energy (dimensionless).

2.2.1. Model validation

Several specific codes were implemented using *Mathematica*[™] software to determine the parameters (the optimal pitch (e_t), the periods of operation of a horizontal single-axis tracker, the optimal number of solar trackers and the power output of a *PV* power plant). A *Mathematica*[™] code was developed to determine the components (beam component, diffuse component, reflected component) of the solar irradiance incident on the *PV* modules, which takes into account the effect of the meteorological conditions at the site. The procedure proposed in Barbón et al. (2020) is the basis of this *Mathematica*[™] code, which was then adapted to the current study. The solar irradiation data, monthly-averaged beam, and diffuse solar irradiation are provided at the *PVGIS* website (PVGIS, 2024).

The validation of the model was carried out from several perspectives: validation using *PVSyst* software (*PVSyst* version 7.2 2024) and experimental validation. For the validation of the model from these points of view, the outdoor facilities of the laboratory of the *CEDS* research group were used. This laboratory is part of the Department of Electrical Engineering at the University of Oviedo in Gijón, Spain (Latitude $43^\circ 31' 22''\text{N}$, Longitude $05^\circ 43' 07''\text{W}$, elevation 28 (m) above sea level). At this location, a prototype horizontal single-axis tracker, as illustrated in Fig. 6, was used to validate the model.

This prototype has a limited range of motion of $\pm 60^\circ$, and comprises mainly the following components: (i) eight photovoltaic modules, (ii) a *DC* motor and controllers, and (iii) an electronic control module. The measurement of the incident solar irradiance on the *PV* field was carried out using a pyranometer, whose specifications are as follows: Type TR1 (Kipp & Zonen), a thermopile sensor, range: $0\text{--}2000$ (W/m^2), and precision/resolution: 1 (W/m^2) (Kipp and Zonen, 2024).

As the solar irradiance is measured directly with the pyranometer, the uncertainty of the measurement is defined by the accuracy of the measuring device (Li et al., 2015). As the uncertainty level is $<2\%$, the measurements are considered acceptable (Al-Waeli et al., 2019). The test conditions were as follows: (i) the test duration was 12 months (2022) and (ii) the pyranometer records values every second with a time step of 1 (min) per integration.

Fig. 7 shows the monthly values of incident solar irradiance on the *PV* field, obtained with: the test, the *Mathematica*[™] code, and the *PVSyst* software.

The differences shown in Fig. 7 between the three procedures are due to the following factors:

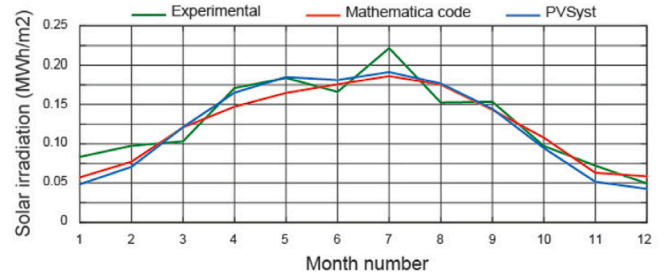


Fig. 7. Comparison of results: test, *Mathematica*[™] code, and *PVSyst* software.

Table 4

Results obtained with Experimental, *Mathematica* and *PVSyst* software.

	Solar irradiation (MWh/m^2)	<i>AIEC</i> (%)
Experimental	1.551	–
<i>PVSyst</i>	1.4730	5.03
<i>Mathematica</i>	1.4772	4.76

- (i) The test was conducted over the year 2022 and the other two procedures used solar irradiance data averaged over a 10-year period. This explains the notable difference in the month of July.
- (ii) The movement of the solar tracker is characterised by its discretisation, i.e. it is not a continuous movement. In contrast, Eq. (4) used in the *Mathematica*[™] code to determine the solar irradiation by integration, is a continuous function (The same is true for the *PVSyst* software). Therefore, both procedures differ from the experimental results.

Eq. (10) was used to compare the annual results:

$$AIEC = \frac{AIE_{Experimental} - AIE_*}{AIE_{Experimental}} \cdot 100 \quad (10)$$

where *AIEC* is the comparison of the annual incident energy on the *PV* field (%), $AIE_{Experimental}$ is the annual incident energy on the *PV* field obtained in the test (MWh/m^2), and AIE_* is the annual incident energy on the *PV* field using *PVSyst* software or *Mathematica*[™] code (MWh/m^2). Table 4 shows the comparison of results using the *PVSyst* software, *Mathematica*[™] codes, and Experimental test. The results using *Mathematica*[™] codes or *PVSyst* software are lower than the values obtained in the experimental test.

The results using *Mathematica*[™] codes are similar to those obtained with the *PVSyst* software, as the difference is less than 0.3% and can therefore be considered insignificant. The results obtained allow us to affirm that the *Mathematica*[™] codes developed are suitable for application in this study.

2.3. Output power of a *PV* power plant

The power output of a *PV* power plant is strongly dependent on the electrical efficiency of the *PV* modules.

The decrease in electrical efficiency of a *PV* module is strongly dependent on its operating temperature (Fouad et al., 2017). It was established that an increase of 1 ($^\circ\text{C}$) of the operating temperature implies a decrease of approximately 0.5% in the electrical efficiency of the module (Fouad et al., 2017). The operating temperature of the module depends, among other factors, on the solar irradiance and the ambient temperature. Increases in these two parameters lead to an increase in *PV* module temperature (Du et al., 2013). The electrical efficiency of a *PV* module can be determined using the equation proposed by Evans (1981):

$$\eta_e = \eta_{ref} \cdot [1 - \beta_{ref} \cdot (T_c - T_{ref})] \quad (11)$$

where η_{ref} is the electrical efficiency at given values of temperature and incident irradiance on the *PV* module (dimensionless), β_{ref} is the

temperature coefficient of the *PV* module ($1/^{\circ}\text{C}$), T_c is the *PV* cell temperature ($^{\circ}\text{C}$), and T_{ref} is the reference temperature ($^{\circ}\text{C}$). The reference temperature established by the *STC* (Standard Test Conditions) is 25 ($^{\circ}\text{C}$) and the reference solar irradiance established by the same conditions is 1000 (W/m^2). The parameters η_{ref} and β_{ref} are provided in the *PV* module data sheet. Due to its simplicity and the availability of the parameters, the Evans equation is used in similar studies such as: in the thermal management of ultra-high concentration photovoltaic cells (Abo-Zahhad et al., 2024), in the study of the effect of flow rate on the performance of the water-based flat-plate photovoltaic-thermal (FPT) system using an analytical technique (Abdul-Ganiyu et al., 2021). Finally, the cell temperature T_c can be determined using *NOCT* (Normal Operating Cell Temperature). Mattei et al. (2006) proposed the following equation:

$$T_c = T_a + (NOCT - 20) \cdot \frac{I_t}{800} \quad (12)$$

where T_a is the ambient temperature ($^{\circ}\text{C}$), *NOCT* is estimated for a reference solar irradiance of 800 (W/m^2), a reference ambient temperature of 20 ($^{\circ}\text{C}$), and a reference wind speed at a *PV* module height of 1 (m/s). The Eq. (12) is often used in similar studies, such as in the modelling of temperature losses in photovoltaic cells (Santiago et al., 2018), or in the strategic assessment of the energy performance of building-integrated photovoltaic systems (Costanzo et al., 2018).

2.4. Structural analysis of a *PV* mounting system

The structural analysis includes the main components of a *PV* mounting system, which are: the central pillar, the pillars, the shaft and the purlins.

Wind action plays a key role in the design of *PV* module mounting systems, especially in mounting systems with rotary movement. Various building codes and standards are used to design *PV* mounting systems so they can withstand the different loads induced on them. The following standards shall be used for structural calculations: (i) CTE DB-SE-A (STBC, 2006), (ii) CTE DB-SE-AE: 2006 (STBC, 2006), (iii) UNE-EN 1990: 2019 (2019) (UNE, 1990), (iv) UNE-EN 1991-1-7: 2018 (2018) (UNE, 1991), (v) UNE-EN 1993-1-9:2013 (2013) (UNE, 1993), (vi) UNE-EN ISO 1461:2010 (2010) (UNE, 1461), and (vii) UNE-EN ISO 14713-1:2017 (2017) (UNE, 14713). The *CTE* (Technical Building Code) (STBC, 2006) is the standard for determining wind and snow loads on structures, and therefore the standard to be used in the design of *PV* mounting systems. Other similar studies base the structural design of *PV* mounting systems on the *CTE* methodology, such as in the design of ground-mounted *PV* power plants (Barbón et al., 2022), or in the optimal design of single-axis tracking *PV* power plants (Barbón et al., 2023a).

It is important to calculate the mounting system to ensure that the *PV* modules will remain attached to the structure during windstorms, and that additional snow loads or combinations of loads do not exceed the structural capacity of the mounting system. The steel structure of a horizontal single-axis tracker is designed to withstand the following loads throughout its lifetime: (i) its own weight, (ii) the weight of the *PV* modules, (iii) the weight of accumulated snow, (iv) the wind load, and (v) the combination of the above loads. Each of these points will be discussed below:

- (i) The load produced by the weight of the structure. The self-weight of the structure can be calculated directly with any structural analysis software.
- (ii) The load produced by the weight of the *PV* modules. Eq. (13) was used to estimate this load:

$$q_{PV} = \frac{W_{ePV}}{A_{PV}} \quad (13)$$

where q_{PV} is the load due to the weight of the *PV* modules (kg/m^2), W_{ePV} is the weight of the *PV* module (kg) and A_{PV} is the area of a *PV* module (m^2).

- (iii) The load produced by the weight of accumulated snow. The location (latitude and longitude), the altitude of the *PV* plant, and the distribution of the accumulated snow load (the concentration of the snow load is considered negligible) are needed to perform these calculations. Thus, the snow load is obtained with these data found in annex E of the code CTE DB-SE-AE: 2006 (STBC, 2006).
- (iv) The load produced by the wind. The calculation process, shown in the code CTE DB-SE-AE (STBC, 2006), uses the equation (STBC, 2006):

$$q_e = q_b \cdot C_e \cdot C_p \cdot C_{prob} \quad (14)$$

where q_e is the static pressure (kN/m^2), q_b is the basic velocity pressure for the reference speed established in the code (kN/m^2) (Annex D of the CTE DB-SE-AE (STBC, 2006) shows the equation to determine q_b), C_e is the exposure factor defined in Table D.2 CTE DB-SE-AE (STBC, 2006), C_p is the pressure coefficient defined in Paragraph D.3 CTE DB SE-AE (STBC, 2006), and C_{prob} is the probability factor defined in Annex D.1 of CTE DB-SE-AE (STBC, 2006).

- (v) A combination of the above loads. Load combinations are detailed in the code CTE DB-SE-A (STBC, 2006). Table 5 shows these combinations, where W_{eS} is the weight of the structure, W_{ePV} is the weight of the *PV* module, S_L is the snow load and W_L is the wind load. The structural components are calculated in the design process to determine the critical scenarios shown in Table 5. The Ultimate Limit State combinations are used to calculate the section dimensions considering the maximum resistance of the profiles and their joints. Serviceability limit state combinations are used to calculate section dimensions considering existing strains and foundation dimensions.

Although the foundations of *PV* mounting systems is an important aspect to be studied in detail, all mounting systems in this study use the same system regardless of the maximum angle of movement of the horizontal single-axis tracker, namely the driven piles (Gonvarri, 2024).

The structures that make up the *PV* mounting system were calculated using the AutoDesk Robot Structural Analysis software (AutoDesk, 2024), as it allows the performance of the *PV* mounting system to be simulated under different types of loads. This software is frequently used for these types of calculations in ground-mounted *PV* power plants (Barbón et al., 2022), or in single-axis tracking *PV* power plants (Barbón et al., 2023a). Annex A contains a summary of the most important results of the structural study.

3. Problem formulation

This section presents the most important aspects related to the need for the study. These aspects are as follows:

- (i) Influence of the maximum angle of movement on the effective annual energy incident on the *PV* field. The incident energy on the *PV* field is the main indicator of the profitability of a *PV* power plant project. Fig. 7 shows indirectly the influence of β_{max} on the annual effective incident energy on the *PV* field. It is not true in all the cases studied that the higher the value of β_{max} , the higher the incident energy on the *PV* field. This is a very important aspect, which indicates that a comparative study of different β_{max} is necessary before choosing the value of this parameter.
- (ii) Influence of wind and snow loads on the maintenance costs of a *PV* power plant. According to a report by renewable energy insurance provider GCube (GCube, 2024) on a study conducted in the United States between 2011 and 2015, 49.8% of *PV* system claims were due to weather-related incidents (action of wind loads). In contrast, electrical failures accounted for 9%. Other studies show the increased impact of weather-related disasters on *PV* systems (Pickerel, 2018). The choice of the maximum angle of movement is related to the effect of wind and snow loads on the *PV* module mounting system (Gonvarri, 2024).

Table 5
Classification of load combinations (STBC, 2006).

Designation	Ultimate limit state	Designation	Serviceability limit state
ULS 1	$1.35 \cdot (W_{es} + W_{epv})$	SLS 1	$(W_{es} + W_{epv})$
ULS 2	$1.35 \cdot (W_{es} + W_{epv}) + 1.5 \cdot W_L + 0.75 \cdot S_L$	SLS 2	$(W_{es} + W_{epv}) + W_L + 0.5 \cdot S_L$
ULS 3	$0.8 \cdot (W_{es} + W_{epv}) + 1.5 \cdot W_L$	SLS 3	$(W_{es} + W_{epv}) + W_L$
ULS 4	$1.35 \cdot (W_{es} + W_{epv}) + 0.9 \cdot W_L + 1.5 \cdot S_L$	SLS 4	$(W_{es} + W_{epv}) + 0.6 \cdot W_L + S_L$

- (iii) Influence of the maximum angle of movement on the cost of the PV module mounting system. Economic criteria have taken precedence in the design of photovoltaic mounting systems, as they have evolved towards increasingly slimmer structures and, therefore, more susceptible to aerostatic effects. This makes it necessary to modify certain design parameters, such as the limit angle of movement, favouring the structural design over the energy aspect. On the other hand, it is true that the higher the β_{max} , the greater the mechanical stresses that the tracker must withstand (Gonvarri, 2024). And finally, the higher the β_{max} , the higher the cost of the tracker. Sometimes high wind loads condition the choice of β_{max} . Therefore, the energy loss must be known for each β_{max} , which will depend on the location of the PV power plant.
- (iv) Influence of the maximum angle of movement on the CO₂ emission. The higher the β_{max} , the higher the weight of the PV module mounting system, and therefore the higher the CO₂ emissions.

It can be concluded that the choice of β_{max} of a PV module mounting system has opposing selection criteria. Therefore, it is necessary to know the influence of β_{max} on a given PV power plant, in the project phase, before selecting the final parameters.

The following starting parameters were considered as constant: the available land area, the shape of the land (rectangular shape), the orography of the land (flat land), the configuration of the mounting system (horizontal single-axis tracker), and the commercial model of the PV module (LR5-72HBD 535 (LONGI)), as they do not influence the stated objective.

Several specific codes were implemented with Mathematica™ software for the detailed analysis of the movement limit of a horizontal single-axis tracker. It must be taken into account that none of the existing commercial software (PVSist, PV*SOL, etc.) on the market allow for such a study in-depth.

4. Limitations of the study

The limitations of this study are related to various aspects of PV power plant design. These limitations are as follows:

- (i) Limitations related to the calculation of wind and snow loads. The five case studies are located in Spain. Spain uses the Spanish Technical Building Code (STBC, 2006) for the calculation of wind and snow loads. On the other hand, if the study were to be carried out in Egypt, the ECP-201 code 2012 would have to be used, and if the location were in Thailand, the code to be used would be the DPT Standard 1311-50 (DPT, 2012). Therefore, the procedure used could be implemented in another location by applying the corresponding standard.
- (ii) Limitations related to the topography of the surface of the PV power plant. The current study is limited to horizontal surfaces and therefore the orientation of the solar tracker will be in a north-south direction. If the PV power plant were located on sloping terrain with an azimuth angle different from 0 (°), it would be necessary to use the appropriate equations to take into account the tilt angle of the terrain and the azimuth angle of the terrain.

- (iii) Limitations related to the knowledge of meteorological data of the location. Obviously, if the meteorological data of the location under study are not known, it will not be possible to calculate the incident irradiance on the PV field. It is true that these data are known for most of the locations in the world.

The inclusion of the above limitations does not mean that the procedure cannot be implemented for other locations.

5. Assessment indicators

This section describes the evaluation indicators used to assess the influence of β_{max} on a horizontal single-axis tracker in the design of a PV power plant.

The electrical power output of a horizontal single-axis tracker depends on several factors, such as the available solar irradiance, the power of the PV module, the electrical efficiency of the PV module, the number of PV modules comprising the solar tracker, the E – W distance between columns of two adjacent mounting systems, the minimum E – W distance between two adjacent mounting systems, the maximum tilt angle, etc. Given the large number of parameters involved in the design of a PV plant, the study was focused on the β_{max} , so that all other parameters would remain constant.

Taking into account energy, environmental and economic aspects in the development of a PV plant project, the following assessment indicators were selected: the annual incident energy on PV modules, the CO₂ emissions, the cost analysis of a PV mounting system, and LCOE efficiency.

5.1. Annual incident energy on PV modules

Using Eqs. (4) and (8) we have developed specific codes, implemented with Mathematica™ software and validated, were used to determine the annual energy incident on PV modules. The annual incident energy rate (AIER) of a PV power plant will be used to analyse the deviation with a horizontal single-axis tracker with a movement limit of ±60 (°). This relationship is defined as:

$$AIER = \frac{AIE_*}{AIE_{60}} \tag{15}$$

where AIER is the annual incident energy ratio, AIE* is the annual incident energy in a PV mounting system with a movement limit of β_{max}^* (±50 to ±59 (°)), and AIE₆₀ is the annual incident energy in a PV mounting system with a movement limit of ±60 (°).

5.2. CO₂ emissions

Steel is the main component in the manufacture of a PV mounting system. The iron and steel industry is a significant emitter of CO₂. Iron and steel accounts for 6–8% of global CO₂ emissions (Bataille, 2020). Estimates show that 1.8 tonnes of CO₂ are emitted into the atmosphere for every tonne of steel produced in the most efficient of processes (Hasanbeigi et al., 2016). However, the global average is roughly 2.3 (t) CO₂/t steel (Hasanbeigi et al., 2016). The Eq. (16) shows the connection between the CO₂ emissions created and the material used to manufacture the PV mounting system (Hasanbeigi et al., 2016):

$$2.3(t)CO_2/(t)steel \tag{16}$$

Furthermore, according to EN ISO1461:2010 (UNE-EN ISO 1461:2010, 2010), between 0.1 and 0.33 (kg) equivalent CO₂ is produced per kg

of steel protected. The Eq. (17) shows the connection between the CO₂ emissions and the protective treatment of the steel used to manufacture of the PV mounting system (UNE-EN ISO 1461:2010, 2010):

$$0.33(\text{kg})\text{CO}_2/(\text{kg})\text{steel} \quad (17)$$

In order to determine the CO₂ emissions, the weight of the steel comprising a PV mounting system must be known. This is determined by the structural analysis of a PV mounting system shown in Section 2. The material used to manufacture of the profiles is shown in Annex B. The same annex also shows the weight of the profiles for each location under study. The profiles used in the PV power plants have a hot-dip galvanised surface treatment.

To assess the CO₂ emissions indicator, the ratio between the CO₂ emissions from the manufacturing process of a PV mounting system with a movement limit * and a PV mounting system with a movement limit of ±60 (°) was used. Eq. (18) shows this relationship:

$$\text{CO}_2ER = \frac{\text{CO}_2E_* - \text{CO}_2E_{60}}{\text{CO}_2E_{60}} \cdot 100 \quad (18)$$

where CO₂ER is the CO₂ emissions ratio, CO₂E* is the CO₂ emissions of the manufacturing process of a PV mounting system with a movement limit of β_{max}* (±50 to ±59 (°)), and CO₂E₆₀ is the CO₂ emissions of the manufacturing process of a PV mounting system with a movement limit of ±60 (°).

5.3. Cost analysis of a PV mounting system

The cost of the PV mounting systems represents a substantial part of the initial investment costs of a large-scale PV plant (Hernández Moro and Martínez Duart, 2013). Trends show that the influence of the cost of PV mounting systems on the total cost is increasing, as the cost of PV modules decreases (Pvinsights, 2022) and the increase of raw materials used to manufacture PV mounting systems increases (MEPS, 2018). The weight of the different components of the PV mounting system determines the cost. For this purpose, the profiles comprising the PV mounting system must be calculated by means of a structural study (Section 2).

The costs of a PV mounting system include the costs of the profiles and the costs of the auxiliary components. The profiles used in the manufacture of a PV mounting system are shown in Annex B. The same annex also shows the cost of the profiles for each location under study. The auxiliary components of a PV mounting system include a large number of elements such as Barbón et al. (2023a): joint shafts, pillar bearings, motor brackets, antenna brackets, shock absorbers, end clamps, clamps, screws, nuts, washers, etc. Annex D shows the cost of the auxiliary components.

The ratio between the cost of the PV mounting system with a movement limit * and a PV mounting system with a movement limit of ±60 (°) was used to assess the cost of the PV mounting system indicator. Eq. (18) shows this relationship:

$$\text{CMSR} = \frac{\text{CMS}_* - \text{CMS}_{60}}{\text{CMS}_{60}} \cdot 100 \quad (19)$$

where CMSR is the cost of the PV mounting system ratio, CMS* is the cost of the PV mounting system with a movement limit of β_{max}* (±50 to ±59 (°)) (€), and CMS₆₀ is the cost of the PV mounting system with a movement limit of ±60 (°) (€).

5.4. LCOE efficiency

The assessment of the economic viability of the choice of the movement limit on a horizontal single-axis tracker is a crucial element when making an investment decision. The aim of the economic feasibility study is to measure the economic performance of each possible movement limit of a horizontal single-axis tracker. For this purpose, the levelised cost of electricity produced (LCOE) can be calculated. This method is used to compare the costs of different power generation

technologies (Aldersey-Williams and Rubert, 2019), or PV mounting systems (Barbón et al., 2023a). LCOE calculations are usually based on the life-cycle cost of the PV system and the energy produced over its lifetime. LCOE in (€/kWh) can be expressed by (Branker et al., 2011):

$$\text{LCOE} = \frac{\sum_{i=0}^N [C_i / (1+r)^i]}{\sum_{i=0}^N [E_i / (1+r)^i]} \quad (20)$$

where *i* is the year number ranging from 0 to *N*, *N* the total lifetime of the project (years), *C_i* is the net cost of the project for *i* (€), *E_i* is the total electrical energy output for *i* (kWh), and *r* is the discount rate for *i*. The initial investment cost, operating and maintenance costs, and interest costs, if applicable, give the net cost of the project. The costs of a horizontal single-axis tracker include the costs of the PV mounting system (see Annexes B and D), the cost of the PV modules (see Annex B) and the cost of the control system and motor (see Annex C).

The total electrical energy output at the *i*th year (*E_i*) could be calculated as follows:

$$E_i = (\tau \cdot \alpha)_i \cdot H_i \cdot \eta_e \cdot (1 - d_r)^i \quad (21)$$

where $\tau \cdot \alpha$ is the product of the transmittance of the glazing and the absorbance of the photovoltaic coating at the *i*th year (dimensionless), *H_i* is the solar irradiation at the *i*th year (kWh), η_e is the electrical efficiency (dimensionless) at the *i*th year, *d_r* is the annual degradation rate, and *i* is the year. *H_i* has been calculated using Eq. (8). The electrical efficiency has been calculated using Eq. (11).

Based on the concept of LCOE, several studies operate with the term 'LCOE efficiency', such as in the numerical study of the influence of terrain slope on the performance of single-axis trackers (Barbón et al., 2023b), the optimal design of PV power plants with single-axis tracking (Barbón et al., 2023a), or in the characterisation of solar absorber coatings for the CSP industry (Boubault et al., 2016). This parameter has been found to facilitate the comparison of different PV mounting systems, solar tracking systems, etc.

Adapting this term to this study, the LCOE efficiency can be defined as the ratio between the LCOE* for a horizontal single-axis tracker with a movement limit of β_{max}* (±50 to ±59 (°)) and the LCOE for a horizontal single-axis tracker with a limit of movement of ±60 (°):

$$\eta_{\text{LCOE}} = \frac{\text{LCOE}_*}{\text{LCOE}_{60}} \quad (22)$$

Notice that an η_{LCOE} value greater than 1 implies that a horizontal single-axis tracker with a movement limit of β_{max}* is less efficient than a horizontal single-axis tracker with a movement limit of ±60 (°).

LCOE results depend on country-specific economic variables, technical variables related to the technology used, etc. Therefore, in order to make the comparison as accurate as possible, a number of assumptions need to be made:

- (i) Only the cost of a horizontal single-axis tracker (the cost of the structure, the cost of the PV modules, the cost of the control system and motor, the cost of auxiliary components) was taken into account in the initial investment cost. In other words, the study is done per tracker.
- (ii) The discount rates are country specific. The study presented is framed in Spain, where the discount rate from 1 January 2024 to 31 March 2024 was 4.11% (European Commission, 2024).
- (iii) The electrical efficiency of a PV module depends on the incident solar irradiance and the operating temperature of the PV module. These two variables are the same in each location analysed in this study, meaning the electrical efficiency is considered the same for each location.
- (iv) As the horizontal single-axis tracker is exposed to the same weather conditions, irrespective of the movement limit used, the parameter *d* is assumed to be the same, 0.5%.

Table 6
Specifications of the PV power plants and locations assessed in this study.

Specifications	PV power plant		
	Canredondo	Miraflores	Basir
Location	Canredondo, (Spain)	Castuera, (Spain)	Medina Sidonia, (Spain)
Latitude	40°47'58.886"N	38°46'4.8"N	36°20'24"N
Longitude	2°31'26.95"W	5°32'49.199"W	5°50'32.6"W
Altitude (m)	1162	389	104
Power (MWp)	21.98	22	20.013
PV mod. number	41 084	41 122	37 408
PV mod. model	LR5-72HBD 535 (LONGI)	LR5-72HBD 535 (LONGI)	LR5-72HBD 535 (LONGI)
PV mod. dim. (mm)	2256 × 1133	2256 × 1133	2256 × 1133
Tracking type	Horiz. single-axis tracker	Horiz. single-axis tracker	Horiz. single-axis tracker
Type of control	Astronomical algorithm	Astronomical algorithm	Astronomical algorithm
Rotation angle	$\beta_{\max} = \pm 60$ (°)	$(\beta_{\max} = \pm 60$ (°))	$(\beta_{\max} = \pm 60$ (°))
Configuration	1 V	1 V	1 V
Pitch (e_i) (m)	5100	6500	6000
Reflectance (ρ_g)	0.2	0.2	0.2
Specifications	Other locations		
	Rubió	Sueca	
Location	Rubió, Lleida (Spain)	Sueca, Valencia (Spain)	
Latitude	42°22'33"N	39°12'09"N	
Longitude	1°13'21"E	0°18'40"W	
Altitude (m)	1628	12	
Power (MWp)	–	–	
PV mod. number	–	–	
PV mod.model	LR5-72HBD 535 (LONGI)	LR5-72HBD 535 (LONGI)	
PV mod. dim. (mm)	2256 × 1133	2256 × 1133	
Tracking type	Horiz. single-axis tracker	Horiz. single-axis tracker	
Type of control	Astronomical algorithm	Astronomical algorithm	
Rotation angle	Up to 120 (°) ($\beta_{\max} = \pm 60$ (°))	Up to 120 (°) ($\beta_{\max} = \pm 60$ (°))	
Configuration	1 V	1 V	
Pitch (e_i) (m)	6000	6000	
Reflectance (ρ_g)	0.2	0.2	

- (v) The report of by National Renewable Energy Laboratory (NREL, 2018) establishes 0.5% of the initial investment cost as the operation and maintenance costs for this type of PV mounting system. Therefore, this value has been assumed in this study.

6. Results and discussions

This section presents the most important results obtained in the study.

According to the proposed assessment indicators, this section shows the main results of the study, for three PV power plants (Canredondo, Miraflores and Basir) located in Spain with different movement limits on a horizontal single-axis tracker, in addition to two locations in Spain that meet the most stringent (Rubió) and most beneficial (Sueca) conditions in terms of wind and snow loads. Ten movement limits for horizontal single-axis trackers were investigated, ranging from ± 50 (°) to ± 60 (°). It should be noted that the three PV power plants have a movement limit of ± 60 (°) (see Table 6). This situation is referred to as the current scenario ($\beta_{\max} = \pm 60$ (°)).

Several specific codes were implemented with *Mathematica*[™] software for the detailed analysis of the movement limit of a horizontal single-axis tracker. It must be taken into account that none of the existing commercial software (PVSist, PV*SOL, etc.) on the market allow for such a study in-depth.

6.1. PV power plants and the locations under study

The energy, environmental and economic impact of the movement limit of horizontal single-axis trackers is studied for three PV power plants at different locations in Spain. The study sites were chosen for their different geographical, climatic, wind load and snow load conditions which would allow a detailed analysis of the impact of the movement limit of horizontal single-axis trackers. In addition, the three PV power plants have different pitch. The geographical and technical

data of the PV power plants under study are listed in Table 6.

To complete the study, two other locations were also chosen, one with the most unfavourable wind load and snow load conditions in Spain (Rubió location), and the other with the most favourable load conditions (Sueca location). The code developed with *Mathematica*[™] software has been used in the 5 locations under study. These locations are shown in Table 6.

The locations under study are shown on several maps under various viewpoints: a global horizontal irradiation map (Fig. 8), a wind zones map (Fig. 10), and a snow zones map (Fig. 11). In addition, the average ambient temperatures of the locations studied are also provided.

Fig. 8 shows the locations on the global irradiance map (SOLARGIS, 2024). The annual global horizontal irradiation at the Canredondo, Miraflores, Basir, Rubió, and Sueca sites is 1687.39 (kWh/m²), 1831.49 (kWh/m²), 1887.12 (kWh/m²), 1618.57 (kWh/m²), and 1768.98 (kWh/m²), respectively.

As already mentioned, the electrical efficiency of a PV module depends on the operating temperature of the PV module. And this parameter, in turn, depends on the solar irradiance and the ambient temperature (Du et al., 2013). Therefore, these two parameters were taken into account in the calculation of the electrical efficiency of a PV module. The ambient temperature at each studied location was obtained from the PVGIS database (PVGIS, 2024). Fig. 9a shows the average ambient temperature of the study locations (PVGIS, 2024). The incident solar irradiance at each location was obtained using the codes implemented with *Mathematica*[™] software.

Fig. 9b shows the monthly electrical efficiency of the studied locations for $\beta_{\max} = \pm 60$ (°).

Fig. 10 shows the locations on the basic wind speed map (STBC, 2006). The basic wind speed at the Canredondo, Miraflores, Basir, Rubió, and Sueca sites is 26 (m/s), 26 (m/s), 29 (m/s), 29 (m/s), and 26 (m/s), respectively.

Fig. 11 shows the locations on the snow zone map (STBC, 2006). The snow overload on horizontal land at the Canredondo, Miraflores, Basir, Rubió, and Sueca sites is 1.767 (kN/m²), 0.295 (kN/m²), 0.200

Table 7
Summary of wind and snow load conditions at study locations (STBC, 2006).

Id	Location	Wind load			Snow load			
		Zone	Wind velocity (m/s)	Categ.	Zone	Altitude (m)	Snow overload (kN/m ²)	Categ.
1	Canredondo	A	26	LI	4	1162	1.767	MI
2	Miraflores	A	26	LI	4	389	0.295	LI
3	Basir	C	29	HI	6	104	0.200	LI
4	Rubió	C	29	HI	2	1628	5.875	HI
5	Sueca	A	26	LI	5	12	0.203	LI

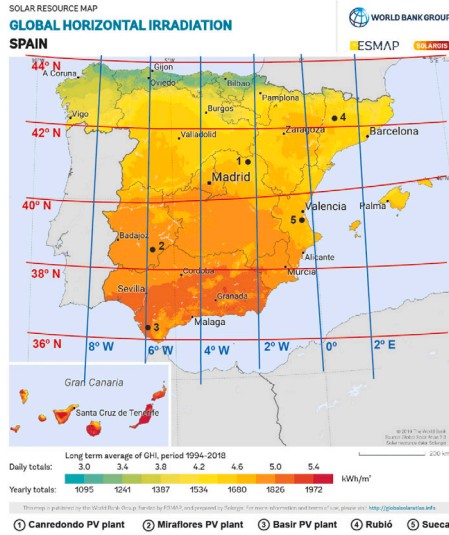


Fig. 8. Map of global irradiation for Spain with the locations under study (SOLARGIS, 2024).

(kN/m²), 5.875 (kN/m²), and 0.203 (kN/m²), respectively.

Table 7 shows the summary of wind and snow load conditions for the locations under study. The impact of these loads was classified according to the following categories: Low Impact (LI), Medium Impact (MI) and High Impact (HI).

In summary, the five locations have been chosen on the basis of the following criteria:

- (i) As can be seen, locations with different levels of global horizontal solar irradiance have been chosen to analyse the influence of the β_{max} on the incident irradiance on the PV field.
- (ii) As shown in Table 6, locations with an altitude difference of more than 1600 (m) have been chosen to analyse the influence of the β_{max} on the altitude of the location.
- (iii) As shown in Fig. 9a, locations with an ambient temperature difference of up to 8 (°C) have been chosen to analyse the influence of the β_{max} on the electrical power generated at each location.
- (iv) As shown in Table 7, locations have been chosen in different snow areas, from the Sueca location with a very low incidence of snow loads, to Rubiό with a very high incidence of snow loads. In order to analyse the influence of the β_{max} on the weight of the PV module mounting system and, therefore, on the cost.
- (v) As shown in Table 7, locations have been chosen in different wind zones, from the Sueca location with a basic wind speed of 26 (m/s) to Rubiό with a basic wind speed of 29 (m/s). In order to analyse the influence of the β_{max} on the weight of the PV module mounting system and, therefore, on the cost.

6.2. Annual incident energy on PV modules

6.2.1. Canredondo PV power plant

The results are shown in Figs. 12 and 13.

Fig. 12a shows the annual incident energy for the movement limits studied. In this location, and also in Miraflores and Basir, to show the non-linear relationship between the variables energy and maximum angle, we use polynomial regression, a versatile and powerful technique to capture these non-linear relationships. We use in Mathematica™ software a nonlinear least-squares model via the NonlinearModelFit function. The coefficient of determination is $R^2 = 1$, and the corrected sums of squares is 8.46852×10^{-7} . In this figure, the maximum annual incident energy corresponds to a movement limit of ± 56 (°). At present, the movement limit of this PV power plant is ± 60 (°) (the current scenario); therefore, the movement limit is not optimised.

Fig. 12b shows the annual incident energy ratio. According to this figure, the adoption of movement limits lower than ± 54 (°) achieves worse results than the current scenario, while the adoption of movement limits of ± 54 (°) or higher achieves better results than the current scenario. Percentage-wise, the AIER is very small yet the energy difference in absolute value is considerable as it depends on the surface of the PV field, which in this PV power plant is 105 012.68 (m²). For example, the incident energy would be 52.51 (MWh) more per year if the movement limit of this PV power plant were ± 56 (°).

Fig. 12c shows the difference between the daily incident energy for $\beta_{max} = \pm 55$ (°) and the current scenario ($\beta_{max} = \pm 60$ (°)). As this figure shows, the movement limit of $\beta_{max} = \pm 55$ (°) performs best on most days. Only in the summer months does the movement limit $\beta_{max} = \pm 60$ (°) perform better. The results of Fig. 12c will be analysed below.

Fig. 13a shows the position of the PV modules on 21 June ($n = 172$) in two scenarios: scenario $\beta_{max} = \pm 55$ (°) (the blue line) and the current scenario ($\beta_{max} = \pm 60$ (°)) (the red line). According to this figure, the two scenarios overlap most of the time, except for the waiting time at the movement limit position. In scenario $\beta_{max} = \pm 55$ (°) (the blue line) this time is longer than in the current scenario (the red line). Although the Sun is above the movement limit, the tracker remains at this limit. This time period will be analysed from various points of view: incident beam irradiance (Fig. 13b), $\cos \theta_i$ (Fig. 13c), and incident diffuse irradiance (Fig. 13d). The component reflected is not analysed as it has a low influence on the incident solar irradiance due to the low value of the albedo.

Fig. 13b shows only the beam component of the incident irradiance during the waiting time at the movement limit position, in the current scenario (the red line) and in the scenario $\beta_{max} = \pm 55$ (°) (the blue line). As can be seen, the current scenario performs better due to the value of $\cos \theta_i$ (see Fig. 13c). However, this better behaviour does not represent a big difference between the two scenarios. Fig. 13c shows the behaviour of $\cos \theta_i$.

Fig. 13d shows only the diffuse component of the incident irradiance during the waiting time at the movement limit position in the current scenario (the red line) and in the $\beta_{max} = \pm 55$ (°) scenario (the blue line). The scenario $\beta_{max} = \pm 55$ (°) performs better, and the difference is noticeable, as the position of $\beta_{max} = \pm 55$ (°) favours the diffuse component. The diffuse component performs worse as it moves away from the 0 (°) tilt angle.

Therefore, it can be concluded that the $\beta_{max} = \pm 55$ (°) scenario favours the diffuse component and the current scenario slightly favours the beam component. Therefore, the $\beta_{max} = \pm 55$ (°) scenario obtains better results than the current scenario.

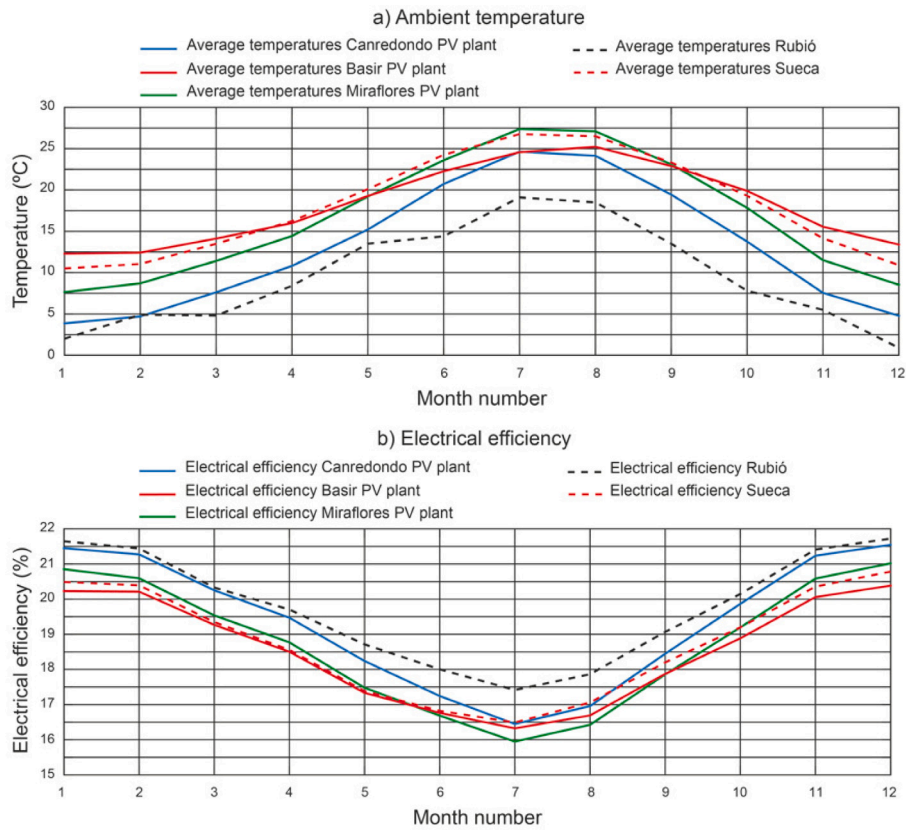


Fig. 9. Average ambient temperature (PVGIS, 2024) and electrical efficiency.

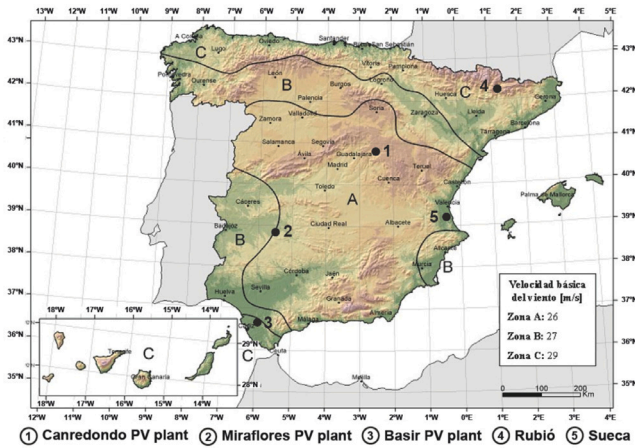


Fig. 10. Map of basic wind velocity for Spain with the locations under study (STBC, 2006).

6.2.2. Miraflores PV power plant

The results are shown in Figs. 14 and 15.

Fig. 14a shows the annual incident energy for the movement limits studied. In this figure, the maximum annual incident energy corresponds to a movement limit of $\pm 60^\circ$, i.e. the current scenario. Therefore, the Miraflores PV power plant uses the optimal movement limit. The coefficient of determination is $R^2 = 1$, and the corrected sums of squares is 2.57854×10^{-5} .

The annual incident energy ratio is shown in Fig. 14b. Based on this figure, the adoption of movement limits lower than $\pm 60^\circ$ increases the energy losses. The increase in energy losses occurs as the movement limit decreases. It is interesting to quantify the energy loss in absolute

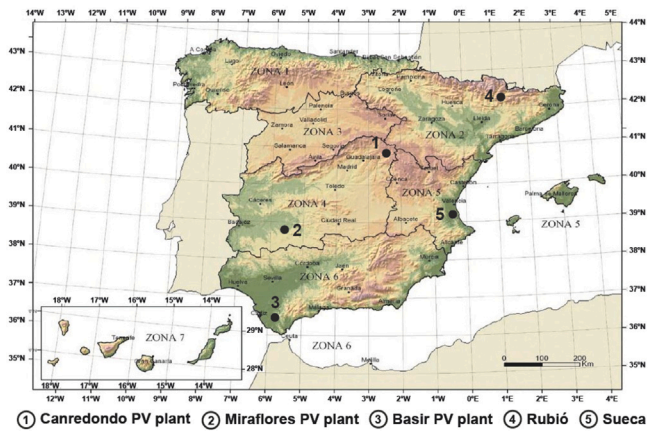


Fig. 11. Map of snow zones for Spain with the locations under study (STBC, 2006).

value even though the *AIER* is quite small as the surface of the PV field is large, particularly for the Miraflores PV power plant where the PV field is 105 109.81 (m²). For example, the incident energy would be 115.62 (MWh) less per year if the movement limit of this PV plant were $\pm 55^\circ$.

The difference between the daily incident energy for scenario $\beta_{max} = \pm 55^\circ$ and the current scenario is shown in Fig. 14c. As this figure shows, the movement limit of $\beta_{max} = \pm 55^\circ$ performs worse every day. The results of Fig. 14c will be analysed below.

The analysis in Fig. 14c will focus on 21 June and two scenarios will be used: scenario $\beta_{max} = \pm 55^\circ$ (the blue line) and the current scenario ($\beta_{max} = \pm 60^\circ$) (the red line). Fig. 15a shows the position of the PV modules under these conditions. This figure shows that the

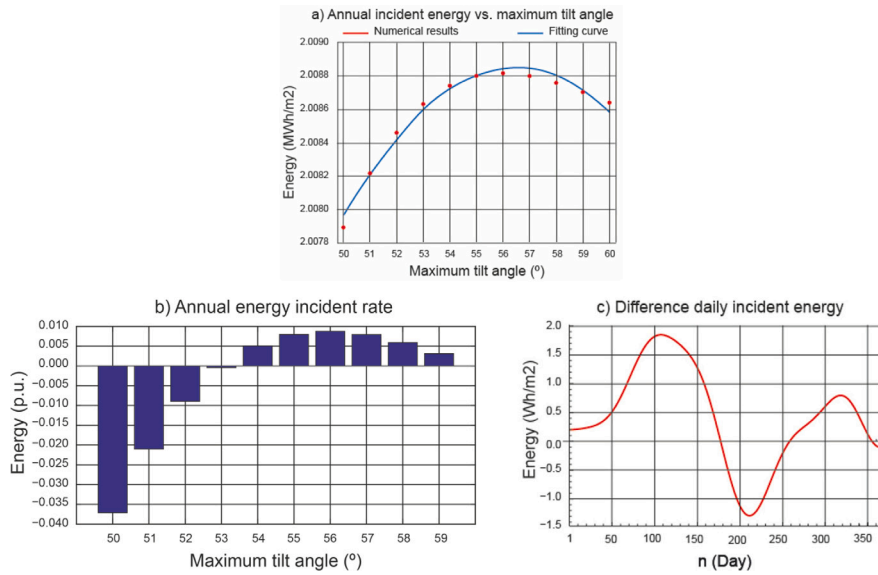


Fig. 12. Incident energy results at the Canredondo PV power plant.

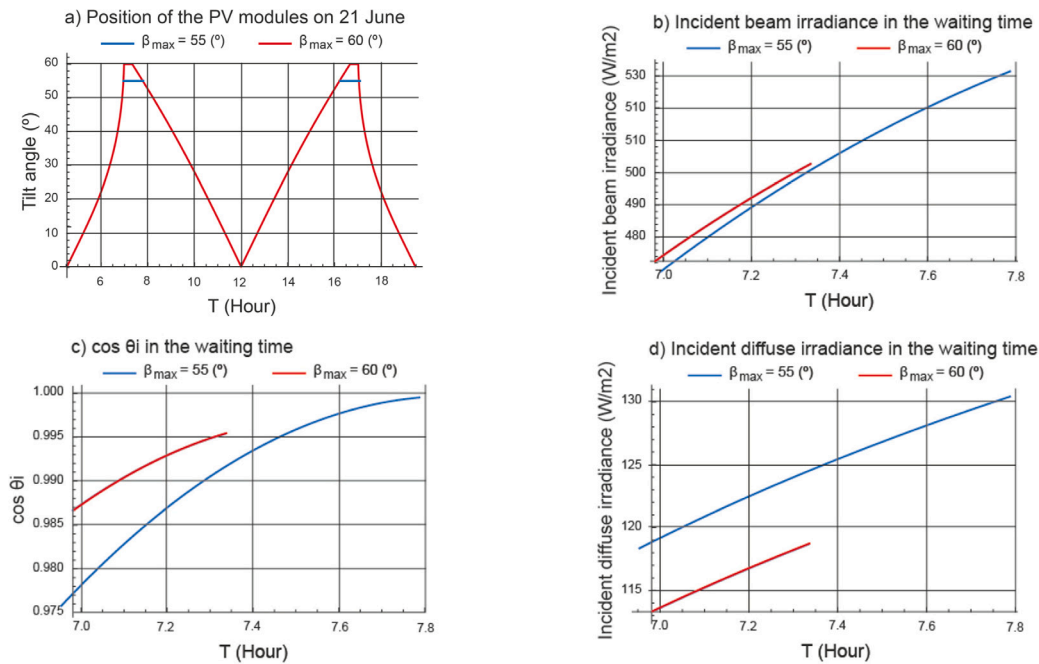


Fig. 13. Position of the PV modules on 21 June at the Canredondo PV power plant.

two scenarios overlap most of the time, except for the waiting time at the movement limit position. In the scenario $\beta_{max} = \pm 55^\circ$ (the blue line), this time is longer than in the current scenario (the red line). This time period will be analysed using several parameters: incident beam irradiance (Fig. 15b), $\cos \theta_i$ (Fig. 15c) and incident diffuse irradiance (Fig. 15d). Due to the low influence of the reflected component on the incident solar irradiance this parameter is not analysed.

Each component of solar irradiance will be analysed separately. The beam component of the irradiance is shown in Fig. 15b. It can be seen that the current scenario performs better due to the value of $\cos \theta_i$ (see Fig. 15c). Moreover, the difference between the two scenarios is remarkable. Fig. 15c shows the behaviour of $\cos \theta_i$.

The diffuse component of the irradiance is shown in Fig. 15d. As the $\beta_{max} = \pm 55^\circ$ scenario favours the diffuse component, it performs better, and the difference is noticeable.

Therefore, the same conclusion obtained for the Canredondo PV power plant can be applied to the Miraflores PV power plant: the $\beta_{max} = \pm 55^\circ$ scenario favours the diffuse component and the current scenario favours the beam component. However, the beam component is predominant at this PV power plant. Therefore, the current scenario obtains better results than the $\beta_{max} = \pm 55^\circ$ scenario.

6.2.3. Basir PV power plant

The results are shown in Figs. 16 and 17.

Fig. 16a shows the annual incident energy as a function of the movement limits under study. According to these results, the maximum annual incident energy corresponds to a movement limit of the current scenario ($\beta_{max} = \pm 60^\circ$). Therefore, the Basir PV power plant uses the optimal movement limit. The coefficient of determination is $R^2 = 1$, and the corrected sums of squares is 1.05319×10^{-5} .

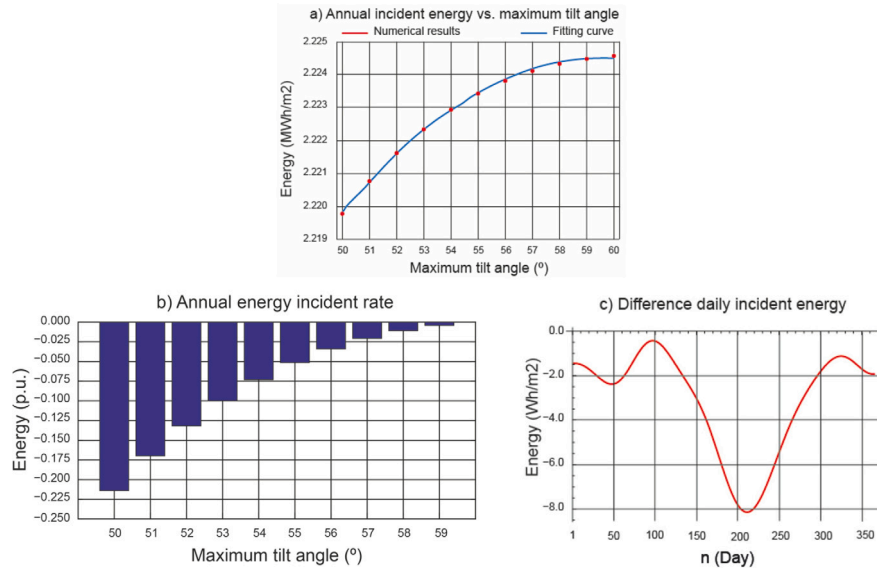


Fig. 14. Incident energy results at the Miraflores PV power plant.

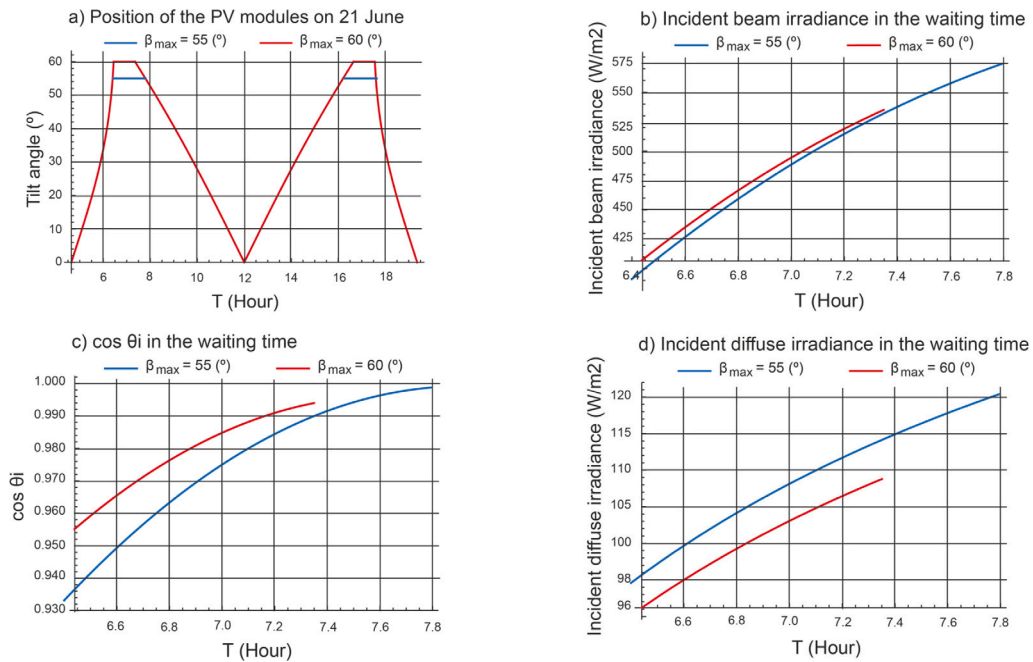


Fig. 15. Position of the PV modules on 21 June at the Miraflores PV power plant.

The annual incident energy ratio is shown in Fig. 16b. According to this figure, the choice of movement limits below $\pm 60^\circ$ increases energy losses. Energy losses increase as the movement limit decreases. As the Basir PV power plant has a PV field of 95616.64 (m²) and although the AIER is very small, it is interesting to quantify the absolute value of the energy loss. Choosing the same movement limit as with the previous PV plants, $\beta_{max} = \pm 55^\circ$, the incident energy would be 47.81 (MWh) less per year.

Fig. 16c shows the difference between the daily incident energy for the scenario $\beta_{max} = \pm 55^\circ$ and the current scenario. As this figure shows, there are very few days per year where the $\beta_{max} = \pm 55^\circ$ scenario performs better. This time period corresponds to autumn. The results in Fig. 16c will be discussed below.

The analysis in Fig. 16c uses the same scenarios as for the previously studied PV power plants ($\beta_{max} = \pm 55^\circ$ (the blue line) and the current scenario (the red line)), and the same study day, 21 June. Fig. 17a

shows the position of the PV modules under these conditions. As is the case with the other PV power plants, the two scenarios overlap most of the time, except for the waiting time at the movement limit position. In the scenario $\beta_{max} = \pm 55^\circ$ (the blue line) this time is longer than in the current scenario (the red line). The analysis of this time period will focus on the following parameters: incident beam irradiance (Fig. 17b), $\cos \theta_i$ (Fig. 17c) and incident diffuse irradiance (Fig. 17d). The component reflected in the incident solar irradiance was not analysed as it is of little relevance.

As in the previous studies, each component of the solar irradiance will be analysed independently. Fig. 17b shows the beam component of the solar irradiance, where the current scenario obtains slightly better results due to the value of $\cos \theta_i$ (see Fig. 17c). But, the difference between the two scenarios is small. Fig. 17c shows the behaviour of $\cos \theta_i$.

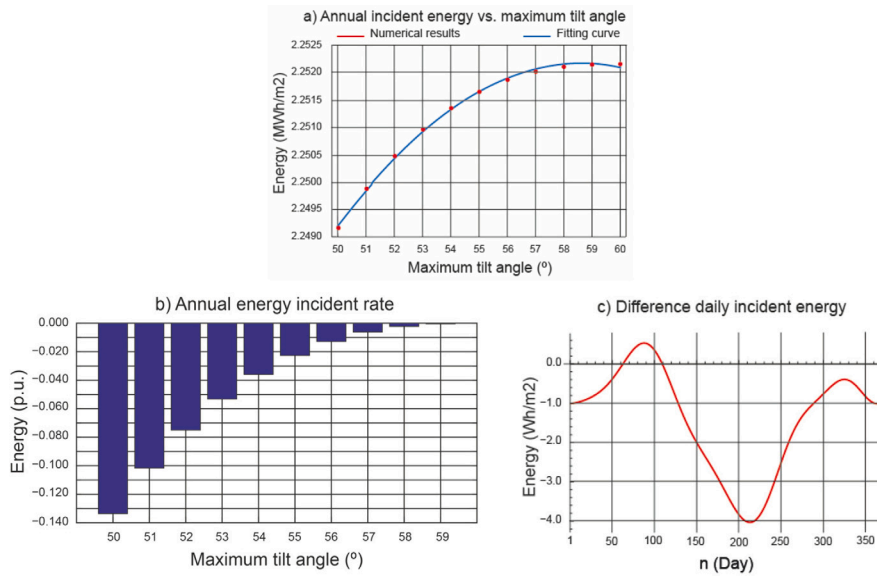


Fig. 16. Incident energy results at the Basir PV power plant.

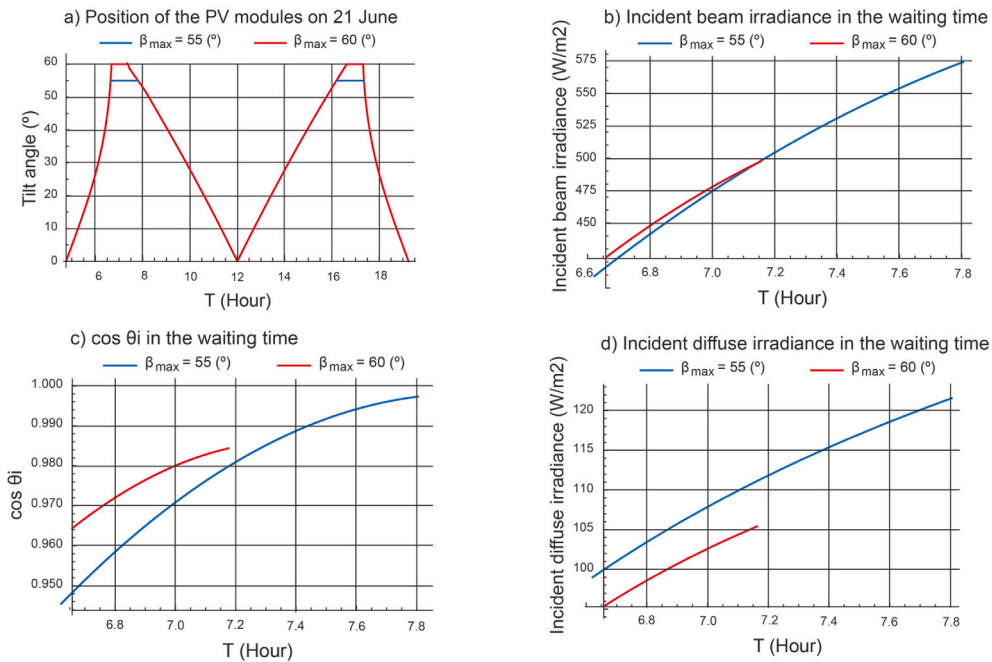


Fig. 17. Position of the PV modules on 21 June at the Basir PV power plant.

Fig. 17d shows the diffuse component of the solar irradiance. As the scenario $\beta_{max} = \pm 55^\circ$ favours the diffuse component, it obtains better results; however, the difference is not very noticeable.

Therefore, the same conclusion obtained with the previously studied plants can be applied to the Basir PV power plant: the scenario $\beta_{max} = \pm 55^\circ$ favours the diffuse component and the current scenario favours the beam component. However, the beam component predominates at this PV power plant. Therefore, the current scenario performs better than the $\beta_{max} = \pm 55^\circ$ scenario.

6.2.4. Rubi3 and sueca locations

Fig. 18a shows the annual incident energy for the movement limits studied at the Rubi3 location. In this figure, the maximum annual incident energy corresponds to a movement limit of $\pm 59^\circ$. If the

general criterion of using a movement limit of $\pm 60^\circ$ were used, the PV system would not be optimised. Fig. 18b shows the annual incident energy ratio at the Rubi3 location. According to this figure, movement limits lower than $\pm 57^\circ$ perform worse than the movement limit of $\pm 60^\circ$, while movement limits of $\pm 58^\circ$ or $\pm 59^\circ$ perform slightly better.

Fig. 18c shows the annual incident energy for the studied movement limits at the Sueca location. In this figure, the maximum annual incident energy corresponds to a movement limit of $\pm 60^\circ$. Therefore, if the general movement limit were to be used in this location, it would be the optimal choice. The annual incident energy ratio is shown in Fig. 18d. According to this figure, movement limits lower than $\pm 60^\circ$ slightly increase the energy losses. This increase in energy losses occurs as the movement limit decreases.

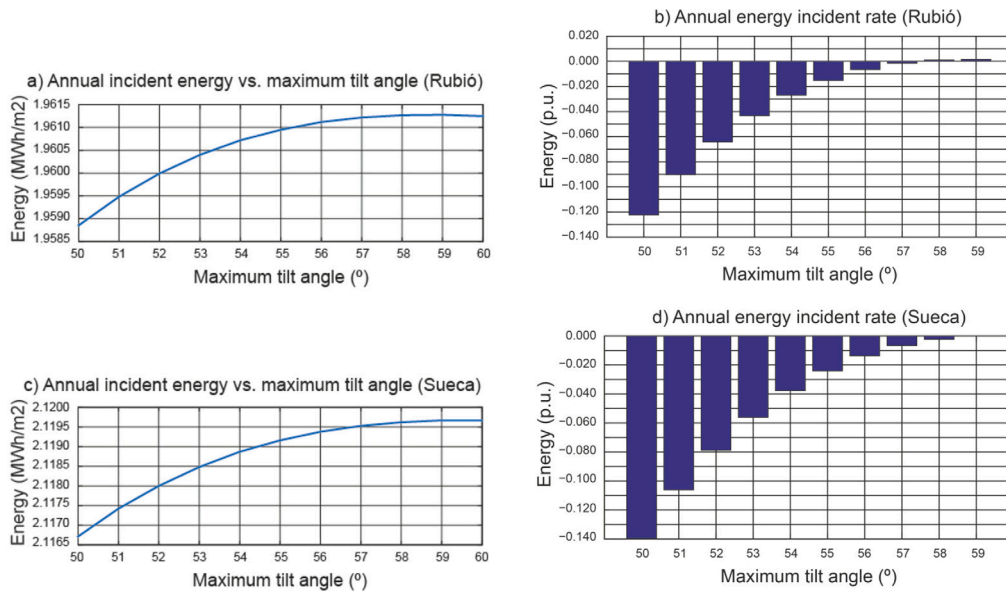


Fig. 18. Incident energy results in Rubiό and Sueca.

Table 8

CO₂ emissions as a function of β_{max} at the study sites.

Location	Canredondo	Miraflores	Basir	Rubiό	Sueca
β_{max} (°)	CO ₂ emissions (t)				
50	3.87	2.58	2.99	4.52	2.58
51	3.87	2.58	2.99	4.52	2.58
52	4.08	2.58	2.99	4.52	2.58
53	4.08	2.61	3.15	4.52	2.61
54	4.16	2.63	3.15	4.67	2.63
55	4.16	2.82	3.15	4.89	2.82
56	4.16	2.91	3.20	5.11	2.91
57	4.64	3.00	3.20	5.11	3.00
58	4.92	3.00	3.20	5.11	3.00
59	4.92	3.00	3.20	5.11	3.00
60	4.92	3.00	3.20	5.11	3.00

Therefore, choosing a movement limit of $\pm 60^\circ$ without performing the corresponding calculations may a priori reduce the benefit of the PV system.

The reduction of incident solar energy was approximately 0.005 (MWh/m²) between the extremes of the movement limits studied. This amount is very noticeable in a large-scale PV power plant, where the PV field can be composed of more than one million PV modules. Therefore, this circumstance has to be taken into account in the design of a PV power plant.

6.3. CO₂ emissions

The CO₂ emissions of the PV mounting system structure were determined using ratios (16) and (17), and Annex B. The CO₂ emissions for each location under study are shown in Table 8.

The following conclusions can be drawn from Table 8:

- (i) The results show a relationship between CO₂ emissions and the presence of wind and snow loads. The higher the impact of wind and snow loads, the higher the CO₂ emissions. Therefore, PV power plants located in areas exposed to high wind and snow loads generate more CO₂ emissions. The Miraflores and Sueca locations, characterised by low wind and snow loads, will be used for comparison with the other locations.
- (ii) At the Canredondo location, characterised by low wind loads and medium snow loads, the configuration $\beta_{max} = \pm 60^\circ$ generates

1.92 (t/tracker) more CO₂ emissions compared to the Miraflores and Sueca locations. And for the configurations $\beta_{max} = \pm 50^\circ$ and $\beta_{max} = \pm 55^\circ$, it generates 1.29 (t/tracker) and 1.34 (t/tracker) more, respectively.

- (iii) At the Basir location, characterised by high wind loads and low snow loads, the configuration $\beta_{max} = \pm 60^\circ$ generates 0.20 (t/tracker) more CO₂ emissions compared to the Miraflores and Sueca locations. And for the configurations $\beta_{max} = \pm 50^\circ$ and $\beta_{max} = \pm 55^\circ$, it generates 0.41 (t/tracker) and 0.33 (t/tracker) more, respectively.

- (iv) At the Rubiό location, characterised by high wind and snow loads, the configuration $\beta_{max} = \pm 60^\circ$ generates 2.11 (t/tracker) more CO₂ emissions compared to the Miraflores and Sueca locations. And for the configurations $\beta_{max} = \pm 50^\circ$ and $\beta_{max} = \pm 55^\circ$, it generates 1.94 (t/tracker) and 2.07 (t/tracker) more, respectively. These results demonstrate point (i).

The results of CO₂ ER are shown in Fig. 19.

The following conclusions can be drawn from Fig. 19:

- (i) The results show that CO₂ emissions decrease with decreasing β_{max} , at all study locations.
- (ii) At the Miraflores and Sueca locations, characterised by low wind and snow loads, the $\beta_{max} = \pm 60^\circ$ configuration generates 13.88% and 5.92% more CO₂ emissions compared to the $\beta_{max} = \pm 50^\circ$ and $\beta_{max} = \pm 55^\circ$ configuration, respectively.
- (iii) At the Canredondo location, characterised by low wind loads and medium snow loads, the $\beta_{max} = \pm 60^\circ$ configuration generates 21.42% and 15.43% more CO₂ emissions compared to the $\beta_{max} = \pm 50^\circ$ and $\beta_{max} = \pm 55^\circ$ configuration, respectively.
- (iv) At the Basir location, characterised by high wind loads and low snow loads, the $\beta_{max} = \pm 60^\circ$ configuration generates 6.35% and 1.33% more CO₂ emissions compared to the $\beta_{max} = \pm 50^\circ$ and $\beta_{max} = \pm 55^\circ$ configuration, respectively.
- (v) At the Rubiό location, which is characterised by high wind and snow loads, the $\beta_{max} = \pm 60^\circ$ configuration generates 11.42% and 4.23% more CO₂ emissions compared to the $\beta_{max} = \pm 50^\circ$ and $\beta_{max} = \pm 55^\circ$ configuration, respectively.
- (vi) At all locations under study, the $\beta_{max} = \pm 55^\circ$ configuration achieves lower CO₂ emissions than the $\beta_{max} = \pm 60^\circ$ configuration.

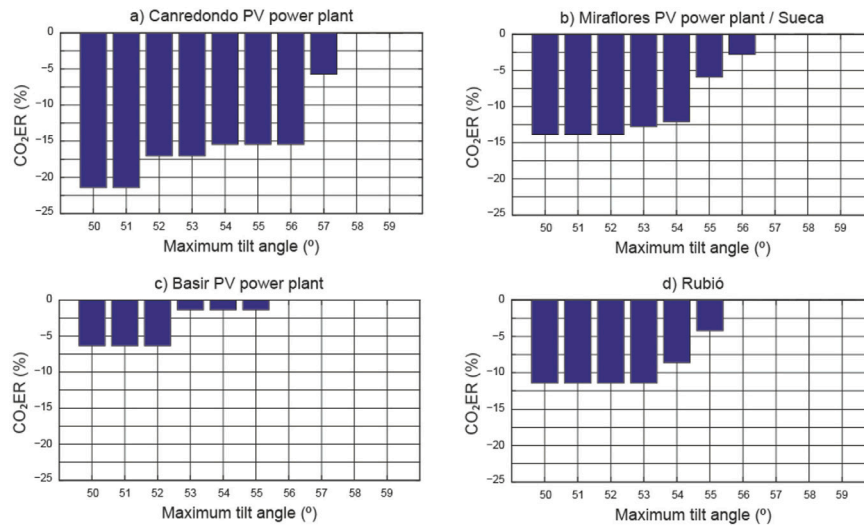


Fig. 19. CO₂ER of the structure.

Table 9
Costs of a PV mounting system as a function of β_{max} at the study sites.

Location	Canredondo	Miraflores	Basir	Rubiό	Sueca
β_{max} (°)	PV mounting system costs (€)				
50	2876.04	2245.42	2450.07	3204.34	2245.42
51	2876.04	2245.42	2450.07	3204.34	2245.42
52	2982.15	2245.42	2450.07	3204.34	2245.42
53	2982.15	2260.95	2526.77	3204.34	2260.95
54	3021.04	2268.45	2526.77	3282.07	2268.45
55	3021.04	2357.91	2526.77	3392.84	2357.91
56	3021.04	2413.93	2553.14	3499.65	2413.93
57	3274.96	2453.91	2553.14	3499.65	2453.91
58	3413.95	2453.91	2553.14	3499.65	2453.91
59	3413.95	2453.91	2553.14	3499.65	2453.91
60	3413.95	2453.91	2553.14	3499.65	2453.91

6.4. Cost analysis of a PV mounting system

Annexes B and D show the costs of a PV mounting system. The costs of a PV mounting system for each location under study are shown in Table 9.

The following conclusions can be drawn from Table 9:

- (i) As the cost of the PV module mounting system depends on its weight, as with CO₂ emissions, the results show a relationship between cost and the presence of wind and snow loads. The higher the impact of wind and snow loads, the higher the costs of the PV mounting system. Therefore, PV power plants located in areas exposed to high wind and snow loads have a higher cost. The Miraflores and Sueca locations, characterised by low wind and snow loads, will be used for comparison with the other locations.
- (ii) At the Canredondo location, characterised by low wind loads and medium snow loads, the configuration $\beta_{max} = \pm 60^\circ$ has a higher cost by approximately 960 (€) compared to the Miraflores and Sueca locations. And for the configurations $\beta_{max} = \pm 50^\circ$ and $\beta_{max} = \pm 55^\circ$, the cost is higher by approximately 630 (€) and 607 (€), respectively.
- (iii) At the Basir location, characterised by high wind loads and low snow loads, the configuration $\beta_{max} = \pm 60^\circ$ has a higher cost by approximately 99 (€) compared to the Miraflores and Sueca locations. And for the configurations $\beta_{max} = \pm 50^\circ$ and $\beta_{max} = \pm 55^\circ$, the cost is higher by approximately 204 (€) and 168 (€), respectively.

- (iv) At the Rubiό location, characterised by high wind and snow loads, the configuration $\beta_{max} = \pm 60^\circ$ has a higher cost by approximately 1045 (€) compared to the Miraflores and Sueca locations. And for the configurations $\beta_{max} = \pm 50^\circ$ and $\beta_{max} = \pm 55^\circ$, the cost is higher by approximately 958 (€) and 1034 (€), respectively.

Fig. 20 shows the CMSR results.

The following conclusions can be drawn from Fig. 20:

- (i) The results show that the PV module mounting system cost decreases with decreasing β_{max} , at all study locations.
- (ii) At the Miraflores and Sueca locations, characterised by low wind and snow loads, the $\beta_{max} = \pm 60^\circ$ configuration has a higher cost of 8.50% and 3.91% compared to the $\beta_{max} = \pm 50^\circ$ and $\beta_{max} = \pm 55^\circ$ configurations, respectively.
- (iii) At the Canredondo location, characterised by low wind loads and medium snow loads, the $\beta_{max} = \pm 60^\circ$ configuration has a higher cost of 15.76% and 11.51% compared to the $\beta_{max} = \pm 50^\circ$ and $\beta_{max} = \pm 55^\circ$ configuration, respectively.
- (iv) At the Basir location, characterised by high wind loads and low snow loads, the $\beta_{max} = \pm 60^\circ$ configuration has a higher cost of 4.04% and 1.03% compared to the $\beta_{max} = \pm 50^\circ$ and $\beta_{max} = \pm 55^\circ$ configuration, respectively.
- (v) At the Rubiό location, which is characterised by high wind and snow loads, the $\beta_{max} = \pm 60^\circ$ configuration has a higher cost of 8.44% and 3.05% compared to the $\beta_{max} = \pm 50^\circ$ and $\beta_{max} = \pm 55^\circ$ configuration, respectively.
- (vi) At all locations under study, the $\beta_{max} = \pm 55^\circ$ configuration has lower costs than the $\beta_{max} = \pm 60^\circ$ configuration. In line with the above, these results are very important, as large-scale PV power plants can be composed of thousands of solar trackers. Therefore, these results can influence the decision making process for the design of a PV power plant.

6.5. LCOE efficiency

Using the Eqs. (20) and (22) the LCOE efficiency can be determined. The data shown in Fig. 9b were used for the determination of energy generated. Annexes B, C and D show the component costs of a horizontal single-axis tracker. Fig. 21 shows the LCOE efficiency.

The following conclusions can be drawn from Fig. 21:

- (i) At all locations under study, the $\beta_{max} = \pm 55^\circ$ configuration performs better than the $\beta_{max} = \pm 60^\circ$ configuration.

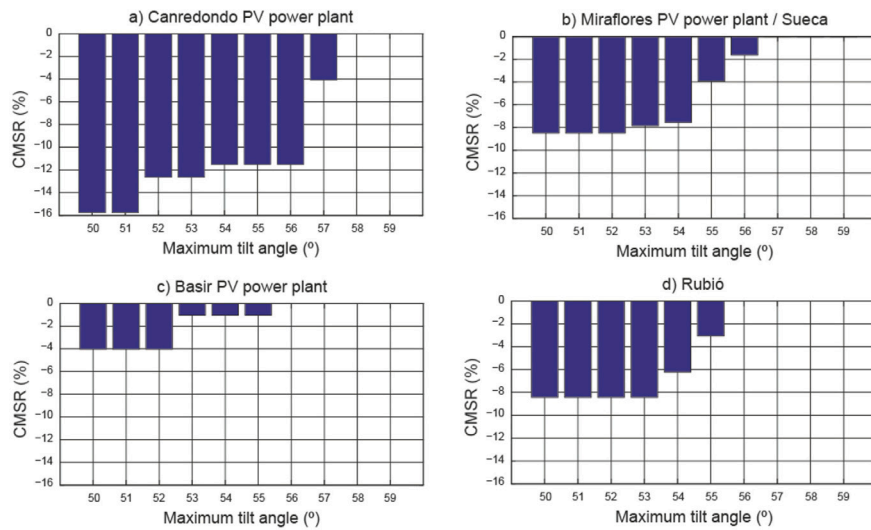


Fig. 20. CMSR of the structure.

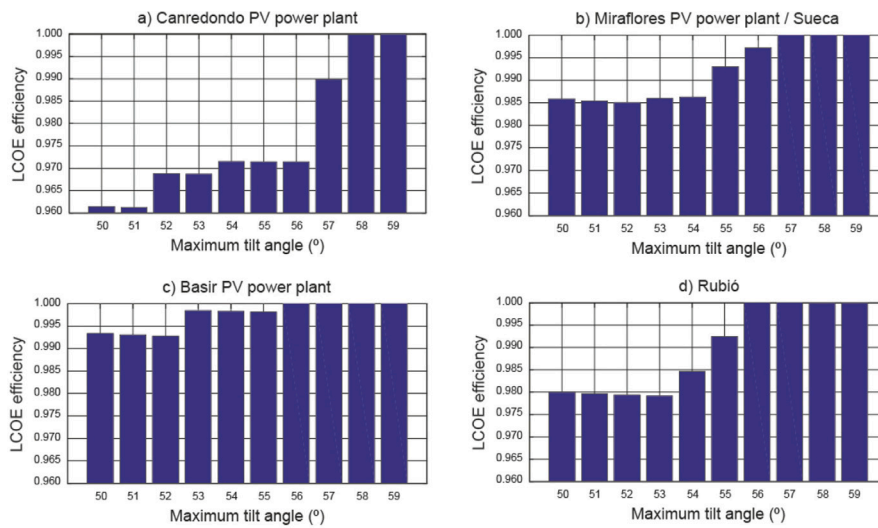


Fig. 21. LCOE efficiency of a horizontal single-axis tracker.

- (ii) At the Miraflores and Sueca locations, characterised by low wind and snow loads, the $\beta_{max} = \pm 52^\circ$ configuration obtains the best *LCOE* efficiency.
- (iii) At the Canredondo location, characterised by low wind loads and medium snow loads, the $\beta_{max} = \pm 51^\circ$ configuration obtains the best *LCOE* efficiency.
- (iii) At the Basir location, characterised by high wind loads and low snow loads, the $\beta_{max} = \pm 52^\circ$ configuration obtains the best *LCOE* efficiency.
- (iv) At the Rubió location, which is characterised by high wind and snow loads, the $\beta_{max} = \pm 53^\circ$ configuration obtains the best *LCOE* efficiency.

7. Conclusions and future works

This paper presents the analysis of the energy, environmental and economic impact of the movement limit on a horizontal single-axis tracker at five locations in Spain: three *PV* power plants (Canredondo, Miraflores and Basir), and the locations of Sueca and Rubió. The study locations were chosen for their different geographical, climatic, wind load and snow load conditions, which allow for a detailed analysis of the impact of the movement limit on horizontal single-axis trackers.

Therefore, four scenarios have been analysed: (i) Scenario 1, characterised by low wind and snow loads (Miraflores *PV* power plant and Sueca location); (ii) Scenario 2, characterised by low wind loads and medium snow loads (Canredondo *PV* power plant); (iii) Scenario 3, characterised by high wind loads and low snow loads (Basir *PV* power plant); and (iv) Scenario 4, characterised by high wind and snow loads (Rubió location). Four evaluation indicators (annual incident energy ratio, CO₂ emissions ratio, *PV* mounting system cost ratio, *LCOE* efficiency) and ten movement limits, ranging from $\pm 50^\circ$ to $\pm 60^\circ$, were analysed. It should be noted that *PV* power plants in Spain generally have a movement limit of $\pm 60^\circ$ (Gonvarri, 2024). Several codes were developed with *Mathematica*TM software to determine the components of the incident solar irradiance (beam component, diffuse component, reflected component), and the periods of operation (normal tracking mode, backtracking mode, and static mode (limited range of movement)) of a horizontal single-axis tracker. A detailed structural analysis of the *PV* mounting system was also carried out, taking into account wind and snow loads. The results show the impact of the choice of the movement limit on a horizontal single-axis tracker at a *PV* power plant. Scenario 1 was used for comparison with the other scenarios. According to this study, the following conclusions can be drawn:

- (i) A study of the movement limit is necessary to optimise the incident energy on the *PV* field at each location, as the value generally used for *PV* power plants of $\pm 60^\circ$ is not optimal at certain locations. In addition, the energy loss that comes with choosing a certain movement limit other than $\pm 60^\circ$ is low.
- (ii) The results show a relationship between CO₂ emissions and the presence of wind and snow loads. The higher the impact of wind and snow loads, the higher the CO₂ emissions. Therefore, *PV* power plants located in areas exposed to high wind and snow loads generate more CO₂ emissions. Furthermore, CO₂ emissions decrease with decreasing β_{max} .
- (a) In Scenario 2, the configurations $\beta_{max} = \pm 50^\circ$, $\beta_{max} = \pm 55^\circ$ and $\beta_{max} = \pm 60^\circ$ generate 1.29 (t/tracker), 1.34 (t/tracker) and 1.92 (t/tracker) more CO₂ emissions compared to Scenario 1.
- (b) In Scenario 3, the configurations $\beta_{max} = \pm 50^\circ$, $\beta_{max} = \pm 55^\circ$ and $\beta_{max} = \pm 60^\circ$ generate 0.41 (t/tracker), 0.33 (t/tracker) and 0.20 (t/tracker) more CO₂ emissions compared to Scenario 1.
- (c) In Scenario 4, the configurations $\beta_{max} = \pm 50^\circ$, $\beta_{max} = \pm 55^\circ$ and $\beta_{max} = \pm 60^\circ$ generate 1.94 (t/tracker), 2.07 (t/tracker) and 2.11 (t/tracker) more CO₂ emissions compared to Scenario 1.
- (iii) The results show a relationship between cost and the presence of wind and snow loads. The higher the impact of wind and snow loads, the higher the costs of the *PV* mounting system. Therefore, *PV* power plants located in areas exposed to high wind and snow loads have a higher cost. In addition, the *PV* module mounting system cost decreases with decreasing β_{max} , at all study locations.
- (a) In Scenario 2, the configurations $\beta_{max} = \pm 50^\circ$, $\beta_{max} = \pm 55^\circ$ and $\beta_{max} = \pm 60^\circ$ the cost is higher by approximately 630 (€), 607 (€) and 960 (€) compared to Scenario 1.
- (b) In Scenario 3, the configurations $\beta_{max} = \pm 50^\circ$, $\beta_{max} = \pm 55^\circ$ and $\beta_{max} = \pm 60^\circ$ the cost is higher by approximately 204 (€), 168 (€) and 99 (€) compared to Scenario 1.
- (c) In Scenario 4, the configurations $\beta_{max} = \pm 50^\circ$, $\beta_{max} = \pm 55^\circ$ and $\beta_{max} = \pm 60^\circ$ the cost is higher by approximately 958 (€), 1034 (€) and 1045 (€) compared to Scenario 1.
- (iv) In all scenarios analysed, the *LCOE* efficiency will always be lower for movement limits below $\beta_{max} = \pm 55^\circ$. At each location there will be an optimal β_{max} . For example: In Scenario 1 it is $\beta_{max} = \pm 52^\circ$, in Scenario 2 it is $\beta_{max} = \pm 51^\circ$, in Scenario 3 it is $\beta_{max} = \pm 52^\circ$, and in scenario 4 it is $\beta_{max} = \pm 53^\circ$.

This results, related with CO₂ emissions and *LCOE* efficiency, show the importance of our study in the frame of sustainable production.

In the current study it has been considered that the photovoltaic power plants are deployed in Spain and on a horizontal surface. As future work, a study of locations in different parts of the world would be proposed, with which different regulations related to the study of wind and snow loads would have to be analysed. For example, the following criteria could be used for new locations: (i) The hemisphere where the new study could be conducted would be in the northern hemisphere, as 90% of the world's population lives in this hemisphere (UN, 2022); (ii) To ensure different weather conditions, the selected locations had to have different latitudes. For example, locations with a difference in latitude of approximately 6° ; (iii) The following locations may be suitable for future work: (a) Medellin (Colombia) (Latitude: $06^\circ 14' 38''$ N; Longitude: $75^\circ 34' 04''$ W; Altitude: 1469 (m)); (b) Bangkok (Thailand) (Latitude: $13^\circ 45' 14''$ N; Longitude: $100^\circ 29' 34''$ E; Altitude: 9 (m)); (c) Morelia (Mexico) (Latitude: $19^\circ 42' 10''$ N; Longitude: $101^\circ 11' 24''$ W; Altitude: 1921 (m)); (d) Karachi (Pakistan) (Latitude: $24^\circ 52' 01''$ N; Longitude: $67^\circ 01' 51''$ E; Altitude: 14 (m)); (e) Cairo (Egypt) (Latitude: $30^\circ 29' 24''$ N; Longitude: $31^\circ 14' 38''$ W; Altitude: 41 (m)); (f) Almeria (Spain) (Latitude: $36^\circ 50' 07''$ N; Longitude: $02^\circ 24' 08''$ W; Altitude: 22 (m)); (g) Toronto (Canada) (Latitude: $43^\circ 39' 14''$ N; Longitude: $79^\circ 23' 13''$ W; Altitude: 106 (m)); (h) Wien (Austria) (Latitude: $48^\circ 15' 00''$ N; Longitude: $16^\circ 21' 00''$ E; Altitude: 203 (m)); (i) Hamburg (Germany) (Latitude: $53^\circ 33' 00''$ N; Longitude: $10^\circ 00' 03''$ E;

Altitude: 19 (m)); and (j) Helsinki (Finland) (Latitude: $60^\circ 10' 10''$ N; Longitude: $24^\circ 56' 07''$ E; Altitude: 23 (m))

Another possible line of work is the analysis of the angle of maximum slope on sloping terrain with different orientations. This would require the derivation of new design equations for the photovoltaic power plant.

CRediT authorship contribution statement

A. Barbón: Methodology, Conceptualization. **V. Carreira-Fontao:** Writing – review & editing, Writing – original draft, Software, Methodology, Conceptualization. **L. Bayón:** Methodology, Conceptualization. **G. Spagnuolo:** Writing – original draft, Software, Methodology.

Declaration of competing interest

The authors declare that they have no known competing financial interests or personal relationships that could have appeared to influence the work reported in this paper.

Acknowledgements

We wish to thank Gonvarri Solar Steel (Gonvarri, 2024) for their contribution to this paper.

Annex A. Structural analysis loads of the *PV* mounting system

The different standards and the values of the different loads acting on the *PV* mounting system are shown in Tables 10, 11, 12, 13 and 14. The *PV* module (LR5-72HBD 535 (LONGI)) used in this study has a weight of 24 (Kg).

Annex B. Profile properties: material, geometric properties, dimensions, weight and cost

Tables 15, 16, 17, 18, 19 and 20 show the properties (material, dimensions, weight, cost) of the profiles used in the manufacturing of the *PV* mounting system for each location under study. The results shown in these tables were obtained using AutoDesk Robot Structural Analysis software. The profiles received a surface treatment by hot-dip galvanising. The data used in the preparation of the cost study refer to 06/03/2024.

Annex C. Costs of *PV* modules, control system and motor

Table 21 shows the costs of the *PV* modules (Autosolar, 2022), control system and motor (Gonvarri, 2024) used. The data used in the preparation of the cost study refer to 06/03/2024.

Annex D. Cost of auxiliary components of the photovoltaic mounting system

The *PV* mounting system requires a number of auxiliary components: screws, washers, nuts, clamps and end clamps. Table 22 shows these elements and their cost (Gonvarri, 2024). The data used in the preparation of the cost study refer to 06/03/2024.

Data availability

The data that has been used is confidential.

Table 10
Values of the loads acting on the PV mounting system in Canredondo PV plant.

Load	Weight		Snow				Wind			
	-	-	(a)	(b)	(c)	(d)	(d)	(e)	(e)	(e)
β_{max} (°)	q_{PV}		q_b	C_e	$C_{p_pushing}$	$C_{p_suction}$	C_{prob}	$q_{e_pushing}$	$q_{e_suction}$	
±50	9.73	0.121	1.767	0.601	1.93	-1.2	1.4	1	-0.377	0.791
±51	9.73	0.121	1.767	0.601	1.93	-1.2	1.4	1	-0.379	0.788
±52	10.28	0.121	1.767	0.601	1.93	-1.2	1.4	1	-0.381	0.785
±53	10.28	0.121	1.767	0.601	1.93	-1.2	1.4	1	-0.384	0.783
±54	10.48	0.121	1.767	0.601	1.93	-1.2	1.4	1	-0.386	0.781
±55	10.48	0.121	1.767	0.601	1.93	-1.2	1.4	1	-0.388	0.779
±56	10.48	0.121	1.767	0.601	1.93	-1.2	1.4	1	-0.390	0.775
±57	11.68	0.121	1.767	0.601	1.93	-1.2	1.4	1	-0.392	0.773
±58	12.39	0.121	1.767	0.601	1.93	-1.2	1.4	1	-0.394	0.770
±59	12.39	0.121	1.767	0.601	1.93	-1.2	1.4	1	-0.396	0.768
±60	12.39	0.121	1.767	0.601	1.93	-1.2	1.4	1	-0.398	0.766

Table 11
Values of the loads acting on the PV mounting system in Miraflores PV plant.

Load	Weight		Snow				Wind			
	-	-	(a)	(b)	(c)	(d)	(d)	(e)	(e)	(e)
β_{max} (°)	q_{PV}		q_b	C_e	$C_{p_pushing}$	$C_{p_suction}$	C_{prob}	$q_{e_pushing}$	$q_{e_suction}$	
±50	6.49	0.121	0.295	0.601	1.93	-1.2	1.4	1	-0.377	0.791
±51	6.49	0.121	0.295	0.601	1.93	-1.2	1.4	1	-0.379	0.788
±52	6.49	0.121	0.295	0.601	1.93	-1.2	1.4	1	-0.381	0.785
±53	6.58	0.121	0.295	0.601	1.93	-1.2	1.4	1	-0.384	0.783
±54	6.63	0.121	0.295	0.601	1.93	-1.2	1.4	1	-0.386	0.781
±55	7.09	0.121	0.295	0.601	1.93	-1.2	1.4	1	-0.388	0.779
±56	7.33	0.121	0.295	0.601	1.93	-1.2	1.4	1	-0.390	0.775
±57	7.54	0.121	0.295	0.601	1.93	-1.2	1.4	1	-0.392	0.773
±58	7.54	0.121	0.295	0.601	1.93	-1.2	1.4	1	-0.394	0.770
±59	7.54	0.121	0.295	0.601	1.93	-1.2	1.4	1	-0.396	0.768
±60	7.54	0.121	0.295	0.601	1.93	-1.2	1.4	1	-0.398	0.766

Table 12
Values of the loads acting on the PV mounting system in Basir PV plant.

Load	Weight		Snow				Wind			
	-	-	(a)	(b)	(c)	(d)	(d)	(e)	(e)	(e)
β_{max} (°)	q_{PV}		q_b	C_e	$C_{p_pushing}$	$C_{p_suction}$	C_{prob}	$q_{e_pushing}$	$q_{e_suction}$	
±50	7.53	0.121	0.200	0.748	1.93	-1.2	1.4	1	-0.468	0.982
±51	7.53	0.121	0.200	0.748	1.93	-1.2	1.4	1	-0.410	0.978
±52	7.53	0.121	0.200	0.748	1.93	-1.2	1.4	1	-0.474	0.975
±53	7.94	0.121	0.200	0.748	1.93	-1.2	1.4	1	-0.476	0.971
±54	7.94	0.121	0.200	0.748	1.93	-1.2	1.4	1	-0.479	0.968
±55	7.94	0.121	0.200	0.748	1.93	-1.2	1.4	1	-0.481	0.966
±56	8.04	0.121	0.200	0.748	1.93	-1.2	1.4	1	-0.483	0.963
±57	8.04	0.121	0.200	0.748	1.93	-1.2	1.4	1	-0.487	0.960
±58	8.04	0.121	0.200	0.748	1.93	-1.2	1.4	1	-0.490	0.957
±59	8.04	0.121	0.200	0.748	1.93	-1.2	1.4	1	-0.492	0.954
±60	8.04	0.121	0.200	0.748	1.93	-1.2	1.4	1	-0.494	0.951

Table 13
Values of the loads acting on the PV mounting system in Rubió location.

Load	Weight		Snow				Wind			
	-	-	(a)	(b)	(c)	(d)	(d)	(e)	(e)	(e)
β_{max} (°)	q_{PV}		q_b	C_e	$C_{p_pushing}$	$C_{p_suction}$	C_{prob}	$q_{e_pushing}$	$q_{e_suction}$	
±50	11.38	0.121	5.875	0.748	1.93	-1.2	1.4	1	-0.468	0.982
±51	11.38	0.121	5.875	0.748	1.93	-1.2	1.4	1	-0.470	0.978
±52	11.38	0.121	5.875	0.748	1.93	-1.2	1.4	1	-0.474	0.975
±53	11.38	0.121	5.875	0.748	1.93	-1.2	1.4	1	-0.476	0.971
±54	11.74	0.121	5.875	0.748	1.93	-1.2	1.4	1	-0.479	0.968
±55	12.31	0.121	5.875	0.748	1.93	-1.2	1.4	1	-0.481	0.966
±56	12.85	0.121	5.875	0.748	1.93	-1.2	1.4	1	-0.483	0.963
±57	12.85	0.121	5.875	0.748	1.93	-1.2	1.4	1	-0.487	0.960
±58	12.85	0.121	5.875	0.748	1.93	-1.2	1.4	1	-0.490	0.957
±59	12.85	0.121	5.875	0.748	1.93	-1.2	1.4	1	-0.492	0.954
±60	12.85	0.121	5.875	0.748	1.93	-1.2	1.4	1	-0.494	0.951

Table 14
Values of the loads acting on the PV mounting system in Sueca location.

Load	Weight		Snow				Wind			
	-	-	(a)	(b)	(c)	(d)	(d)	(e)	(e)	(e)
β_{max} (°)		q_{PV}		q_b	C_e	$C_{p_pushing}$	$C_{p_suction}$	C_{prob}	$q_{e_pushing}$	$q_{e_suction}$
±50	6.49	0.121	0.203	0.601	1.93	-1.2	1.4	1	-0.377	0.791
±51	6.49	0.121	0.203	0.601	1.93	-1.2	1.4	1	-0.379	0.788
±52	6.49	0.121	0.203	0.601	1.93	-1.2	1.4	1	-0.381	0.785
±53	6.58	0.121	0.203	0.601	1.93	-1.2	1.4	1	-0.384	0.783
±54	6.63	0.121	0.203	0.601	1.93	-1.2	1.4	1	-0.386	0.781
±55	7.09	0.121	0.203	0.601	1.93	-1.2	1.4	1	-0.388	0.779
±56	7.33	0.121	0.203	0.601	1.93	-1.2	1.4	1	-0.390	0.775
±57	7.54	0.121	0.203	0.601	1.93	-1.2	1.4	1	-0.392	0.773
±58	7.54	0.121	0.203	0.601	1.93	-1.2	1.4	1	-0.394	0.770
±59	7.54	0.121	0.203	0.601	1.93	-1.2	1.4	1	-0.396	0.768
±60	7.54	0.121	0.203	0.601	1.93	-1.2	1.4	1	-0.398	0.766

(a) Annex E of the code CTE DB-SE-AE (STBC, 2006); (b) Table D.1 CTE DB SE-AE (STBC, 2006); (c) Table D.2 CTE DB SE-AE (STBC, 2006); (d) UNE-EN 1991-1-7: 2018 (2018) (UNE, 1991); (e) CTE DB-SE-AE code (STBC, 2006).

Table 15
Material and dimensions of profiles used.

Element	Length (mm)	Material	Unit
Central pillar	2440	S 280GD Z275	1
Pillar	2825	S 280GD Z275	8
Central shaft	9900	S 280GD Z275	2
Intermediate shaft 1	8000	S 280GD Z275	2
Intermediate shaft 2	8000	S 280GD Z275	2
Extreme shaft	7800	S 280GD Z275	2
Purlins 1	430	S 280GD Z275	58
Purlins 2	1430	S 280GD Z275	2

Table 16
Cost, weight and geometrical properties of profiles used in Canredondo PV plant.

β_{max} (°)	Central pillar	Pillar	Central shaft	Interm. shaft 1	Interm. shaft 2	Extr. shaft	Purlins 1&2	Weight (kg)	Cost (€)
±50	W8 × 13	C195 × 90 × 30 × 3.5	130 × 4.5	130 × 4.5	130 × 4	130 × 3.5	40 × 50 × 25.1 × 1.6	1471.02	2051.99
±51	W8 × 13	C195 × 90 × 30 × 3.5	130 × 4.5	130 × 4.5	130 × 4	130 × 3.5	40 × 50 × 25.1 × 1.6	1471.02	2051.99
±52	W8 × 13	C195 × 90 × 30 × 3.5	130 × 5	130 × 5	130 × 4	130 × 3.5	40 × 50 × 25.1 × 1.6	1553.18	2158.10
±53	W8 × 13	C195 × 90 × 30 × 3.5	130 × 5	130 × 5	130 × 4	130 × 3.5	40 × 50 × 25.1 × 1.6	1553.18	2158.10
±54	W8 × 13	C195 × 90 × 30 × 3	130 × 5	130 × 5	130 × 4	130 × 4	40 × 50 × 25.1 × 1.6	1583.09	2196.99
±55	W8 × 13	C195 × 90 × 30 × 3.5	130 × 5	130 × 5	130 × 4	130 × 4	40 × 50 × 25.1 × 1.6	1583.09	2196.99
±56	W8 × 13	C195 × 90 × 30 × 3.5	130 × 5	130 × 5	130 × 4	130 × 4	40 × 50 × 25.1 × 1.6	1583.09	2196.99
±57	W8 × 15	C200 × 100 × 30 × 4	130 × 5.5	130 × 5.5	130 × 5	130 × 4	40 × 50 × 25.1 × 1.6	1765.05	2450.91
±58	W8 × 15	C200 × 100 × 30 × 4	130 × 6	130 × 6	130 × 5	130 × 4.5	40 × 50 × 25.1 × 1.6	1872.03	2589.90
±59	W8 × 15	C200 × 100 × 30 × 4	130 × 6	130 × 6	130 × 5	130 × 4.5	40 × 50 × 25.1 × 1.6	1872.03	2589.90
±60	W8 × 15	C200 × 100 × 30 × 4	130 × 6	130 × 6	130 × 5	130 × 4.5	40 × 50 × 25.1 × 1.6	1872.03	2589.90

Table 17
Cost, weight and geometrical properties of profiles used in Miraflores PV plant.

β_{max} (°)	Central pillar	Pillar	Central shaft	Interm. shaft 1	Interm. shaft 2	Extr. shaft	Purlins 1&2	Weight (kg)	Cost (€)
±50	W8 × 13	C195 × 90 × 30 × 3	130 × 2.5	130 × 2.5	130 × 2.3	130 × 2.3	40 × 50 × 25.1 × 1.3	981.28	1421.37
±51	W8 × 13	C195 × 90 × 30 × 3	130 × 2.5	130 × 2.5	130 × 2.3	130 × 2.3	40 × 50 × 25.1 × 1.3	981.28	1421.37
±52	W8 × 13	C195 × 90 × 30 × 3	130 × 2.5	130 × 2.5	130 × 2.3	130 × 2.3	40 × 50 × 25.1 × 1.3	981.28	1421.37
±53	W8 × 13	C195 × 90 × 30 × 3	130 × 2.5	130 × 2.5	130 × 2.5	130 × 2.3	40 × 50 × 25.1 × 1.3	993.85	1436.90
±54	W8 × 13	C195 × 90 × 30 × 3	130 × 2.5	130 × 2.5	130 × 2.5	130 × 2.3	40 × 50 × 25.1 × 1.5	1001.51	1444.41
±55	W8 × 13	C195 × 90 × 30 × 3	130 × 3	130 × 3	130 × 2.5	130 × 2.3	40 × 50 × 25.1 × 1.5	1071.98	1533.86
±56	W8 × 13	C195 × 90 × 30 × 3.5	130 × 3	130 × 3	130 × 2.5	130 × 2.3	40 × 50 × 25.1 × 1.5	1107.94	1589.88
±57	W8 × 13	C195 × 90 × 30 × 3.5	130 × 3	130 × 3	130 × 3	130 × 2.3	40 × 50 × 25.1 × 1.5	1139.44	1629.86
±58	W8 × 13	C195 × 90 × 30 × 3.5	130 × 3	130 × 3	130 × 3	130 × 2.3	40 × 50 × 25.1 × 1.5	1139.44	1629.86
±59	W8 × 13	C195 × 90 × 30 × 3.5	130 × 3	130 × 3	130 × 3	130 × 2.3	40 × 50 × 25.1 × 1.5	1139.44	1629.86
±60	W8 × 13	C195 × 90 × 30 × 3.5	130 × 3	130 × 3	130 × 3	130 × 2.3	40 × 50 × 25.1 × 1.5	1139.44	1629.86

Table 18
Cost, weight and geometrical properties of profiles used in Basir PV plant.

β_{max} (°)	Central pillar	Pillar	Central shaft	Interm. shaft 1	Interm. shaft 2	Extr. shaft	Purlins 1&2	Weight (kg)	Cost (€)
±50	W8 × 15	C195 × 90 × 30 × 4	130 × 3	130 × 3	130 × 3	130 × 2.3	40 × 50 × 25.1 × 1.5	1138.33	1626.02
±51	W8 × 15	C195 × 90 × 30 × 4	130 × 3	130 × 3	130 × 3	130 × 2.3	40 × 50 × 25.1 × 1.5	1138.33	1626.02
±52	W8 × 15	C195 × 90 × 30 × 4	130 × 3	130 × 3	130 × 3	130 × 2.3	40 × 50 × 25.1 × 1.5	1138.33	1626.02
±53	W8 × 15	C195 × 90 × 30 × 4	130 × 3.5	130 × 3.5	130 × 3	130 × 2.3	40 × 50 × 25.1 × 1.5	1199.31	1702.72
±54	W8 × 15	C195 × 90 × 30 × 4	130 × 3.5	130 × 3.5	130 × 3	130 × 2.3	40 × 50 × 25.1 × 1.5	1199.31	1702.72
±55	W8 × 15	C195 × 90 × 30 × 4	130 × 3.5	130 × 3.5	130 × 3	130 × 2.3	40 × 50 × 25.1 × 1.5	1199.31	1702.72
±56	W8 × 15	C195 × 100 × 30 × 3.5	130 × 3.5	130 × 3.5	130 × 3	130 × 2.3	40 × 50 × 25.1 × 1.5	1215.53	1729.09
±57	W8 × 15	C195 × 100 × 30 × 3.5	130 × 3.5	130 × 3.5	130 × 3	130 × 2.3	40 × 50 × 25.1 × 1.5	1215.53	1729.09
±58	W8 × 15	C195 × 100 × 30 × 3.5	130 × 3.5	130 × 3.5	130 × 3	130 × 2.3	40 × 50 × 25.1 × 1.5	1215.53	1729.09
±59	W8 × 15	C200 × 100 × 30 × 3.5	130 × 3.5	130 × 3.5	130 × 3	130 × 2.3	40 × 50 × 25.1 × 1.5	1215.53	1729.09
±60	W8 × 15	C200 × 100 × 30 × 3.5	130 × 3.5	130 × 3.5	130 × 3	130 × 2.3	40 × 50 × 25.1 × 1.5	1215.53	1729.09

Table 19
Cost, weight and geometrical properties of the profiles used on the Rubió location.

β_{max} (°)	Central pillar	Pillar	Central shaft	Interm. shaft 1	Interm. shaft 2	Extr. shaft	Purlins 1&2	Weight (kg)	Cost (€)
±50	W8 × 18	C200 × 100 × 30 × 3.5	130 × 5.5	130 × 5.5	130 × 4.5	130 × 4	40 × 60 × 25.1 × 1.8	1720.30	2380.28
±51	W8 × 18	C200 × 100 × 30 × 3.5	130 × 5.5	130 × 5.5	130 × 4.5	130 × 4	40 × 60 × 25.1 × 1.8	1720.30	2380.28
±52	W8 × 18	C200 × 100 × 30 × 3.5	130 × 5.5	130 × 5.5	130 × 4.5	130 × 4	40 × 60 × 25.1 × 1.8	1720.30	2380.28
±53	W8 × 18	C200 × 100 × 30 × 3.5	130 × 5.5	130 × 5.5	130 × 4.5	130 × 4	40 × 60 × 25.1 × 1.8	1720.30	2380.28
±54	W8 × 18	C200 × 100 × 30 × 4	130 × 5.5	130 × 5.5	130 × 4.5	130 × 4	40 × 65 × 29 × 2	1774.87	2458.02
±55	W8 × 18	C200 × 100 × 30 × 4	130 × 5.5	130 × 5.5	130 × 5	130 × 4.5	41 × 65 × 29 × 2	1860.08	2568.79
±56	W8 × 18	C200 × 100 × 30 × 4	130 × 6	130 × 6	130 × 5	130 × 4.5	41 × 65 × 29 × 2	1942.24	2675.60
±57	W8 × 18	C200 × 100 × 30 × 4	130 × 6	130 × 6	130 × 5	130 × 4.5	41 × 65 × 29 × 2	1942.24	2675.60
±58	W8 × 18	C200 × 100 × 30 × 4	130 × 6	130 × 6	130 × 5	130 × 4.5	41 × 65 × 29 × 2	1942.24	2675.60
±59	W8 × 18	C200 × 100 × 30 × 4	130 × 6	130 × 6	130 × 5	130 × 4.5	41 × 65 × 29 × 2	1942.24	2675.60
±60	W8 × 18	C200 × 100 × 30 × 4	130 × 6	130 × 6	130 × 5	130 × 4.5	41 × 65 × 29 × 2	1942.24	2675.60

Table 20
Cost, weight and geometrical properties of profiles used in Sueca location.

β_{max} (°)	Central pillar	Pillar	Central shaft	Interm. shaft 1	Interm. shaft 2	Extr. shaft	Purlins 1&2	Weight (kg)	Cost (€)
±50	W8 × 13	C195 × 90 × 30 × 3	130 × 2.5	130 × 2.5	130 × 2.3	130 × 2.3	40 × 50 × 25.1 × 1.3	981.28	1421.37
±51	W8 × 13	C195 × 90 × 30 × 3	130 × 2.5	130 × 2.5	130 × 2.3	130 × 2.3	40 × 50 × 25.1 × 1.3	981.28	1421.37
±52	W8 × 13	C195 × 90 × 30 × 3	130 × 2.5	130 × 2.5	130 × 2.3	130 × 2.3	40 × 50 × 25.1 × 1.3	981.28	1421.37
±53	W8 × 13	C195 × 90 × 30 × 3	130 × 2.5	130 × 2.5	130 × 2.5	130 × 2.3	40 × 50 × 25.1 × 1.3	993.85	1436.90
±54	W8 × 13	C195 × 90 × 30 × 3	130 × 2.5	130 × 2.5	130 × 2.5	130 × 2.3	40 × 50 × 25.1 × 1.5	1001.51	1444.41
±55	W8 × 13	C195 × 90 × 30 × 3	130 × 3	130 × 3	130 × 2.5	130 × 2.3	40 × 50 × 25.1 × 1.5	1071.98	1533.86
±56	W8 × 13	C195 × 90 × 30 × 3.5	130 × 3	130 × 3	130 × 2.5	130 × 2.3	40 × 50 × 25.1 × 1.5	1107.94	1589.88
±57	W8 × 13	C195 × 90 × 30 × 3.5	130 × 3	130 × 3	130 × 3	130 × 2.3	40 × 50 × 25.1 × 1.5	1139.44	1629.86
±58	W8 × 13	C195 × 90 × 30 × 3.5	130 × 3	130 × 3	130 × 3	130 × 2.3	40 × 50 × 25.1 × 1.5	1139.44	1629.86
±59	W8 × 13	C195 × 90 × 30 × 3.5	130 × 3	130 × 3	130 × 3	130 × 2.3	40 × 50 × 25.1 × 1.5	1139.44	1629.86
±60	W8 × 13	C195 × 90 × 30 × 3.5	130 × 3	130 × 3	130 × 3	130 × 2.3	40 × 50 × 25.1 × 1.5	1139.44	1629.86

Table 21
Costs of the control system and motor.

Element	Units	Total cost (€)
PV module model (LR5-72HBD 535 (LONGI))	58	9610.02
Slewdrive (motor)	1	437.80
TCU (Tracker Control Unit)	1	108.95

Table 22
Costs of the other elements.

Element	Standard	Material	Surface treatam.	Units	Total cost (€)
Joint shafts	–	–	HD G*	6	40.26
Pillar bearing	–	–	HD G*	6	91.74
Motor supp,	–	–	HD G*	1	28.00
Antenna supp,	–	–	HD G*	1	0.87
TCU* supp,	–	–	HD G*	2	10.62
NCU* supp,	–	–	HD G*	2	74.82
NCU* supp,	–	–	HD G*	2	179.58
RCU* supp,	–	–	HD G*	1	217.34
RSU* supp,	–	–	HD G*	1	40.01
Damper	–	–	–	4	140.8
End clamp	DIN 933	Aluminium	–	8	6.95
Clamp	DIN 933	Aluminium	–	108	136.62
Screw M16 × 40	DIN 6921 8.8	Class 8.8	HD G	72	11.36
Nut M16	DIN 6923 8	Class 8.8	HD G	72	1.56
Screw M16 × 60	DIN 6921 8.8	Class 8.8	HD G	4	0.68
Nut M16	DIN 6923 8	Class 8.8	HD G	4	0.09
Screw M10 × 55	DIN 6921 8.8 4 7	Class 8.8	HD G	24	0.89
Nut M10	DIN 6923 8 4 8	Class 8.8	HD G	24	0.24
Screw M12 × 30	DIN 6921 8.8 4 9	Class 8.8	HD G	24	2.04
Nut M12	DIN 6923 8	Class 8.8	HD G	24	0.98
Screw M16 × 30	DIN 6921 8.8	Class 8.8	HD G	116	19.43
Square U Bolt	SBS-04 1 7	Class 8.8	HD G	58	33.81
Nut M16	DIN 6923 8	Class 8.8	Stainless	116	2.30

References

Abdul-Ganiyu, S., Quansah, D.A., Ramde, E.W., Seidu, R., Adaramola, M.S., 2021. Study effect of flow rate on flat-plate water-based photovoltaic-thermal (PVT) system performance by analytical technique. *J. Clean. Prod.* 321, 128985.

Abo-Zahhad, E.M., Haridy, S., Radwan, A., El-Sharkawy, I.I., Esmail, M.F.C., 2024. Thermal management of ultra high concentrator photovoltaic cells: Analysing the impact of sintered porous media microchannel heat sinks. *J. Clean. Prod.* 465, 142649.

Al-Waeli, A.H.A., Chaichan, M.T., Sopian, K., Kazem, H.A., Mahood, H.B., Khadom, A.A., 2019. Modeling and experimental validation of a PVT system using nanofluid coolant and nano-PCM. *Sol. Energy* 177, 178–191.

Aldersey-Williams, J., Rubert, T., 2019. Levelised cost of energy – A theoretical justification and critical assessment. *Energy Policy* 124, 169–179.

Ali, O.M., Alomar, O.R., 2023. Technical and economic feasibility analysis of a PV grid-connected system installed on a university campus in Iraq. *Environ. Sci. Pollut. Res.* 30, 15145–15157.

Ali, O.M., Alomar, O.R., Mohamed, S.I., 2022. Technical, economical and environmental feasibility study of a photovoltaic system under the climatic condition of north Iraq. *Int. J. Ambient Energy* 44 (1), 212–220.

Alomar, O.R., Ali, O.M., Ali, B.M., Qader, V.S., Ali, O.M., 2023. Energy, exergy, economical and environmental analysis of photovoltaic solar panel for fixed, single and dual axis tracking systems: An experimental and theoretical study. *Case Stud. Therm. Eng.* 51, 103635.

Alves Veríssimo, P.H., Antunes Campos, R., Vivian Guarneri, M., Alves Veríssimo, J.P., do Nascimento, L.R., Rüther, R., 2020. Area and LCOE considerations in utility-scale, single-axis tracking PV power plant topology optimization. *Sol. Energy* 211, 433–445.

Antonanzas, J., Urraca, R., Martínez-de Pison, F.J., Antonanzas, F., 2018. Optimal solar tracking strategy to increase irradiance in the plane of array under cloudy conditions: A study across Europe. *Sol. Energy* 163, 122–130.

Armstrong, S., Hurlley, W.G., 2010. A new methodology to optimise solar energy extraction under cloudy conditions. *Renew. Energy* 35, 780–787.

AutoDesk, 2024. Robot structural analysis software. Available from: <https://www.autodesk.com/products/robot-structural-analysis/overview>. (Accessed 18 July 2024).

Autosolar, 2022. Technical data. Available from: <https://autosolar.es/>. (Accessed 18 July 2024).

Barbón, A., Bayón-Cueli, C., Bayón, L., Carreira-Fontao, V., 2022. A methodology for an optimal design of ground-mounted photovoltaic power plants. *Appl. Energy* 314, 118881.

Barbón, A., Carreira-Fontao, V., Bayón, L., Silva, C.A., 2023a. Optimal design and cost analysis of single-axis tracking photovoltaic power plants. *Renew. Energy* 211, 626–646.

Barbón, A., Fortuny Ayuso, P., Bayón, L., Fernández-Rubiera, J.A., 2020. Predicting beam and diffuse horizontal irradiance using Fourier expansions. *Renew. Energy* 154, 46–57.

Barbón, A., Fortuny Ayuso, P., Bayón, L., Silva, C.A., 2021. A comparative study between racking systems for photovoltaic power systems. *Renew. Energy* 180, 424–437.

Barbón, A., Fortuny Ayuso, P., Bayón, L., Silva, C.A., 2023b. Experimental and numerical investigation of the influence of terrain slope on the performance of single-axis trackers. *Appl. Energy* 348, 121524.

Bataille, C., 2020. Low and Zero Emissions in the Steel and Cement Industries: Barriers, Technologies and Policies. OECD Green Growth Papers, No. 2020/02, OECD Publishing, Paris.

Belhachat, F., Larbes, C., 2015. Modeling, analysis and comparison of solar photovoltaic array configurations under partial shading conditions. *Sol. Energy* 120, 399–418.

Blanco-Muriel, M., Alarcon-Padilla, D.C., Lopea-Moratalla, T., Lara-Coira, M., 2001. Computing the solar vector. *Sol. Energy* 70, 431–441.

Boubault, A., Ho, C.K., Hall, A., Lambert, T.N., Ambrosini, A., 2016. Levelized cost of energy (LCOE) metric to characterize solar absorber coatings for the CSP industry. *Renew. Energy* 85, 472–483.

Branker, K., Pathak, M.J.M., Pearce, J.M., 2011. A review of solar photovoltaic levelized cost of electricity. *Renew. Sustain. Energy Rev.* 15, 4470–4482.

Casares de la Torre, F.J., Varo, M., López-Luque, R., Ramírez-Faz, J., Fernández-Ahumada, L.M., 2022. Design and analysis of a tracking / backtracking strategy for PV plants with horizontal trackers after their conversion to agrivoltaic plants. *Renew. Energy* 187, 537–550.

Costanzo, V., Yao, R., Essah, E., Shao, L., Shahrestani, M., Oliveira, A.C., Araz, M., Hepbasli, A., Biyik, E., 2018. A method of strategic evaluation of energy performance of building integrated photovoltaic in the urban context. *J. Clean. Prod.* 184, 82–91.

2012. Dpt standard 1311-50.

Du, D., Darkwa, J., Kokogiannakis, G., 2013. Thermal management systems for photovoltaics (PV) installations: A critical review. *Sol. Energy* 97, 238–254.

Duffie, J.A., Beckman, W.A., 2013. *Solar Engineering of Thermal Processes*, fourth ed. John Wiley & Sons, New York.

ECP-201, 2012. Egyptian Code of Practice for Calculation of Loads and Forces in Structures and Buildings. National Housing and Building Research Center, Cairo.

Energy Institute, 2023. Statistical Review of World Energy, seventy-second ed. Available from: <https://www.energyinst.org/statistical-review>. (Accessed 18 July 2024).

European Commission, 2024. Available from: <https://competition-policy.ec.europa.eu/state-aid/legislation/reference-discount-rates-and-recovery-interest-rates/reference-and-discount-rates.en>. (Accessed 18 July 2024).

Evans, D.L., 1981. Simplified method for predicting photovoltaic array output. *Sol. Energy* 27, 555–560.

FMI, Future Market Insights, 2023. Solar trackers market: Solar trackers market analysis by single-axis and dual-axis for 2023 to 2033. Available from: <https://www.futuremarketinsights.com/reports/solar-trackers-market#:~:text=The%20global%20solar%20trackers%20market,to%20renewable%20energy%20sources%20grows>. (Accessed 18 July 2024).

Fouad, M.M., Shihata, L.A., Morgan, E.I., 2017. An integrated review of factors influencing the performance of photovoltaic panels. *Renew. Sustain. Energy Rev.* 80, 1499–1511.

GCube, 2024. Available from: <https://www.gcube-insurance.com/en/>. (Accessed 18 July 2024).

Gonvarri Solar Steel, 2024. Available from: <https://www.gsolarsteel.com/>. (Accessed 18 July 2024).

Grena, R., 2008. An algorithm for the computation of the solar position. *Sol. Energy* 82, 462–470.

Hasanbeigi, A., Arens, M., Rojas Cardenas, J.C., Price, L., Triolo, R., 2016. Comparison of carbon dioxide emissions intensity of steel production in China, Germany, Mexico, and the United States. *Resour. Conserv. Recy.* 113, 127–139.

Hay, J.E., 1993. Calculating solar radiation for inclined surfaces: practical approaches. *Renew. Energy* 3, 373–380.

Hernández Moro, J., Martínez Duart, J.M., 2013. Analytical model for solar PV and CSP electricity costs: present LCOE values and their future evolution. *Renew. Sustain. Energy Rev.* 20, 119–132.

Hottel, H.C., 1976. A simple model for estimating the transmittance of direct solar radiation through clear atmosphere. *Sol. Energy* 18, 129–134.

Institute for Energy Diversification and Saving, 2011. Technical Conditions for PV Installations Connected To the Grid [in Spanish]. Spanish Government Technical Report, Available from: <http://www.idae.es>. (Accessed 18 July 2024).

International Energy Agency (IEA), 2023. World energy outlook 2023. Available from: <https://iea.blob.core.windows.net/assets/ed1e4c42-5726-4269-b801-97b3d32e117c/WorldEnergyOutlook2023.pdf>. (Accessed 18 July 2024).

International Renewable Energy Agency (IRENA), 2023. Renewable energy statistics 2023. Available from: https://mc-cd8320d4-36a1-40ac-83cc-3389-cdn-endpoint.azureedge.net/-/media/Files/IRENA/Agency/Publication/2023/Jul/IRENA_Renewable_energy_statistics_2023.pdf?rev=7b2f44c294b84cad9a27fc24949d2134. (Accessed July January 2024).

Jallal, M.A., El Yassini, A., Chabaa, S., Zeroual, A., Ibyaich, S., 2020. Ensemble learning algorithm-based artificial neural network for predicting solar radiation data. In: *IEEE International Conference on Decision Aid Sciences and Application*. DASA, pp. 526–531.

Kalogirou, S.A., Agathokleous, R., Panayiotou, G., 2013. On-site PV characterization and effect of soiling on their performance. *Energy* 51, 439–446.

Keiner, D., Walter, L., ElSayed, M., Breyer, C., 2024. Impact of backtracking strategies on techno-economics of horizontal single-axis tracking solar photovoltaic power plants. *Sol. Energy* 267, 112228.

- Kipp, Zonen, 2024. Available from: <https://www.kippzonen.com/Products>. (Accessed 23 November 2024).
- Li, M., Zhang, Q., Li, G., Shao, S., 2015. Experimental investigation on performance and heat release analysis of a pilot ignited direct injection natural gas engine. *Energy* 90, 1251–1260.
- Liu, B.Y.H., Jordan, R.C., 1960. The interrelationship and characteristic distribution of direct, diffuse and total solar radiation. *Sol. Energy* 4, 1–19.
- Liu, B.Y.H., Jordan, R.C., 1963. The long-term average performance of flat-plate solar energy collectors. *Sol. Energy* 7, 53–74.
- López, M., Soto, F., Hernández, Z.A., 2022. Assessment of the potential of floating solar photovoltaic panels in bodies of water in mainland Spain. *J. Clean. Prod.* 340, 130752.
- Makhdoomi, S., Askarzadeh, A., 2021. Impact of solar tracker and energy storage system on sizing of hybrid energy systems: A comparison between diesel/PV/PHS and diesel/PV/FC. *Energy* 231, 120920.
- Martín-Martínez, S., Cañas-Carretón, M., Honrubia-Escribano, A., Gómez-Lázaro, E., 2019. Performance evaluation of large solar photovoltaic power plants in Spain. *Energy Convers. Manage.* 183, 515–528.
- Martínez-García, E., Blanco-Marigorta, E., Parrondo Gayo, J., Navarro-Manso, A., 2021. Influence of inertia and aspect ratio on the torsional galloping of single-axis solar trackers. *Eng. Struct.* 243, 112682.
- Mattei, M., Notton, G., Cristofari, C., Muselli, M., Poggi, P., 2006. Calculation of the polycrystalline PV module temperature using a simple method of energy balance. *Renew. Energy* 31, 553–567.
- Mehleri, E.D., Zervas, P.L., Sarimveis, H., Palyvos, J.A., Markatos, N.C., 2010. Determination of the optimal tilt angle and orientation for solar photovoltaic arrays. *Renew. Energy* 35, 2468–2475.
- MEPS, MEPS (International) LTD, 2018. Available from: <http://www.meps.co.uk/>. (Accessed 18 July 2024).
- Michalsky, J.J., 1988. The astronomical Almanac's algorithm for approximate solar position (1950–2050). *Sol. Energy* 40, 227–235.
- Mohammed, M.A., Ali, B.M., Yassin, K.F., Ali, O.M., Alomar, O.R., 2024. Comparative study of different phase change materials on the thermal performance of photovoltaic cells in Iraq's climate conditions. *Energy Rep.* 11, 18–27.
- NREL, 2018. Best Practices for Operation and Maintenance of Photovoltaic and Energy Storage Systems, third ed. National Renewable Energy Laboratory, Golden, CO, Available from: <https://www.nrel.gov/docs/fy19osti/73822.pdf>. (Accessed 18 July 2024).
- Perez, R., Ineichen, P., Seals, R., Michalsky, J., Stewart, R., 1990. Modeling daylight availability and irradiance components from direct and global irradiance. *Sol. Energy* 44, 271–289.
- Pfahl, A., Buselmeier, M., Zschke, M., 2018. Wind loads on heliostats and photovoltaic trackers of various aspect ratios. *Sol. Energy* 85, 2185–2201.
- Pickrel, K., 2018. How the solar industry is responding to the increasing intensity of natural disasters. *Solar Power World* Available from: <https://www.solarpowerworldonline.com/2018/01/solar-industry-responding-increasing-intensity-natural-disasters/>. (Accessed July January 2024).
- PVGIS, Joint Research Centre (JRC), 2024. Available from: http://re.jrc.ec.europa.eu/pvg_tools/en/tools.html. (Accessed July January 2024).
- Pvinsights, 2022. Available from: <http://pvinsights.com/>. (Accessed 18 July 2024).
- PVSyst, 2024. Available from: <https://www.pvsyst.com/>. (Accessed 18 July 2024).
- Racharla, S., Rajan, K., 2017. Solar tracking system – a review. *Int. J. Sustain. Eng.* 10, 72–81.
- Reda, I., Andreas, A., 2004. Solar position algorithm for solar radiation applications. *Sol. Energy* 76, 577–589.
- Salazar, G., Gueymard, C., Bezerra Galdino, J., Castro Vilela, O., 2020. Solar irradiance time series derived from high-quality measurements, satellite-based models, and reanalyses at a near-equatorial site in Brazil. *Renew. Sustain. Energy Rev.* 117, 109478.
- Santiago, I., Trillo-Montero, D., Moreno-Garcia, I.M., Pallarés-López, V., Luna-Rodríguez, J.J., 2018. Modeling of photovoltaic cell temperature losses: A review and a practice case in south Spain. *Renew. Sustain. Energy Rev.* 90, 70–89.
- Skoplaki, E., Palyvos, J.A., 2009. On the temperature dependence of photovoltaic module electrical performance: A review of efficiency/power correlations. *Sol. Energy* 83, 614–624.
- SOLARGIS, 2024. Available from: Available from: <https://solargis.com/maps-and-gis-data/download/world>. (Accessed 18 July 2024).
- Stathopoulos, T., Zisis, I., Xypnitou, E., 2014. Local and overall wind pressure and force coefficients for solar panels. *J. Wind Eng. Ind. Aerodyn.* 125, 195–206.
2006. Spanish technical building code royal decree 314/2006.
- Strobel, K., Banks, D., 2014. Effects of vortex shedding in arrays of long inclined flat plates and ramifications for ground-mounted photovoltaic arrays. *J. Wind Eng. Ind. Aerodyn.* 133, 146–149.
- United Nations, 2016. Sustainable development goals. Available from: <https://sdgs.un.org/goals>. (Accessed 18 January 2024).
- United Nations, 2021. Theme report on energy transition. Available from: <https://www.un.org/sites/un2.un.org/files/2021-tw2-062321.pdf>. (Accessed 18 July 2024).
- United Nations, 2022. World population prospects 2022. United Nations. Available from: <https://population.un.org/wpp/>. (Accessed 20 November 2024).
- UNE-EN 1990: 2019, 2019. Basis of Structural Design. AENOR.
- UNE-EN 1991-1-7: 2018, 2018. Actions on Structures. AENOR.
- UNE-EN 1993-1-9:2013, 2013. Design of Steel Structures. AENOR.
- UNE-EN ISO 1461:2010, 2010. Hot Dip Galvanized Coatings on Fabricated Iron and Steel Articles. EANOR.
- UNE-EN ISO 14713-1:2017, 2017. Zinc Coatings - Guidelines and Recommendations for the Protection Against Corrosion of Iron and Steel in Structures. AENOR.
- Yaghoubirad, M., Azizi, N., Ahmadi, A., Zarei, Z., Farhan Moosavian, S., 2022. Performance assessment of a solar PV module for different climate classifications based on energy, exergy, economic and environmental parameters. *Energy Rep.* 8, 15712–15728.
- Yousef, M.S., Sharaf, M., Huzayyin, A.S., 2022. Energy, exergy, economic, and environmental assessment of a photovoltaic module incorporated with a paraffin-metal foam composite: An experimental study. *Energy* 238, 121807.
- Yusuf, A., Astiaso Garcia, D., 2023. Energy, exergy, economic, and environmental (4E) analyses of bifacial concentrated thermoelectric-photovoltaic systems. *Energy* 282, 128921.
- Zhu, Y., Liu, J., Yang, X., 2020. Design and performance analysis of a solar tracking system with a novel single-axis tracking structure to maximize energy collection. *Appl. Energy* 264, 114647.